DISCLAIMER

This report was prepared as an account of work sponsored by an agency of the United States Government. Neither the United States Government nor any agency thereof, nor any of their employees, makes any warranty, express or implied, or assumes any legal liability or responsibility for the accuracy, completeness, or usefulness of any information, apparatus, product, or process disclosed, or represents that its use would not infringe privately owned rights. Reference herein to any specific commercial product, process, or service by trade name, trademark, manufacturer, or otherwise does not necessarily constitute or imply its endorsement, recommendation, or favoring by the United States Government or any agency thereof. The views and opinions of authors expressed herein do not necessarily state or reflect those of the United States Government or any agency thereof. Reference herein to any social initiative (including but not limited to Diversity, Equity, and Inclusion (DEI); Community Benefits Plans (CBP); Justice 40; etc.) is made by the Author independent of any current requirement by the United States Government and does not constitute or imply endorsement, recommendation, or support by the United States Government or any agency thereof.

CASL-U-2017-1447-000

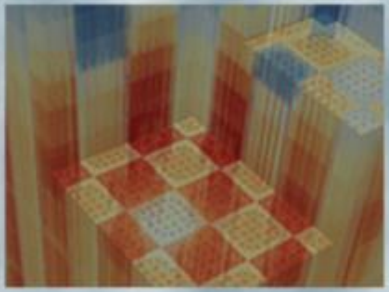

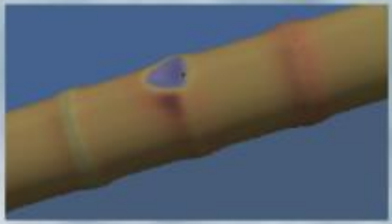

High-to-Low Activities across VVI, AMA and PHI

Ralph C. Smith[2], Brian Williams[1], Maria Avramova[2], Taylor Blyth[2], Kevin Clarno[3], Lindsay Gilkey[4], Natalie Gordon[4], Adam Hetzler[4], Russell Hooper[4], Chris Jones[4], David J. Kropaczek[2], Vincent Mousseau[4], Robert Salko[3], Yixing Sung[5], Emre Tatli[5], and Aysenur Toptan[2]

[1]Los Alamos National Laboratory
[2]North Carolina State University
[3]Oak Ridge National Laboratory
[4]Sandia National Laboratories
[5]Westinghouse Electric Company

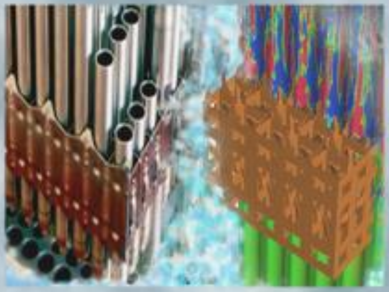

09/30/2017

DOCUMENT AVAILABILITY

Reports produced after January 1, 1996, are generally available free via US Department of Energy (DOE) SciTech Connect.

Website www.osti.gov

Reports produced before January 1, 1996, may be purchased by members of the public from the following source:

National Technical Information Service
5285 Port Royal Road
Springfield, VA 22161
Telephone 703-605-6000 (1-800-553-6847)
TDD 703-487-4639
Fax 703-605-6900
E-mail info@ntis.gov
Website http://classic.ntis.gov/

Reports are available to DOE employees, DOE contractors, Energy Technology Data Exchange representatives, and International Nuclear Information System representatives from the following source:

Office of Scientific and Technical Information
PO Box 62
Oak Ridge, TN 37831
Telephone 865-576-8401
Fax 865-576-5728
E-mail reports@osti.gov
Website http://www.osti.gov/contact.html

This report was prepared as an account of work sponsored by an agency of the United States Government. Neither the United States Government nor any agency thereof, nor any of their employees, makes any warranty, express or implied, or assumes any legal liability or responsibility for the accuracy, completeness, or usefulness of any information, apparatus, product, or process disclosed, or represents that its use would not infringe privately owned rights. Reference herein to any specific commercial product, process, or service by trade name, trademark, manufacturer, or otherwise, does not necessarily constitute or imply its endorsement, recommendation, or favoring by the United States Government or any agency thereof. The views and opinions of authors expressed herein do not necessarily state or reflect those of the United States Government or any agency thereof.

Revision Log

Revision	Date	Affected Pages	Revision Description
0	09/30/2017	All	Initial Release

Document pages that are:

Export Controlled:	None
IP/Proprietary/NDA Controlled:	None
Sensitive Controlled:	None
Unlimited:	All

Requested distribution:

To:

Copy:

EXECUTIVE SUMMARY

This milestone report documents work performed in CASL that was broadly focused on the use of validated high-fidelity simulation codes to inform, improve and calibrate low-fidelity codes to facilitate multiphysics coupling, design, performance analysis, and risk assessment. This high-to-low (Hi2Lo) initiative has the following objectives: employ physics encapsulated in high-fidelity codes to improve the functionality of low-fidelity codes, quantify biases in low-fidelity codes, develop and calibrate physical models and closure relations so that low-fidelity codes more accurately incorporate requisite physics, and develop low-fidelity codes that can be effectively coupled to simulate multiphysics behavior. In combination, these efforts are designed to impact both CIPS and DNB. For example, the development and experimental design-based Bayesian calibration of dynamic gas conductance models in CTFFuel will provide the capability to better model crud-induced power shifts. Whereas the present emphasis has focused on the high-fidelity codes STAR-CCM+ and BISON and low-fidelity codes CTF and CTFFuel, future emphasis will be expanded to include MAMBA.

During the reporting period, Hi2Lo efforts focused on two broad components: demonstration of the experimental design-based Bayesian calibration framework to calibrate CTF using both STAR-generated synthetic data and experimental data, and the use of STAR to inform and improve the turbulence modeling and grid heat transfer modeling capabilities in CTF. A complementary milestone focused on the implementation and verification of fuel models in CTFFuel, for which we demonstrated initial calibration results.

Future Hi2Lo work will focus on the use of the experimental design-based Bayesian calibration framework, demonstrated this year for STAR and CTF, to calibrate parameters in the fuel swelling, fuel irradiation-induced densification, and fuel relocation models in CTFFuel using both experimental and BISON-generated data. A second component will focus on the continued use of STAR to improve grid modeling capabilities in CTF.

(This page intentionally left blank)

CONTENTS

(This page intentionally left blank)

FIGURES

TABLES

ACRONYMS AND INITIALISMS

CASL Consortium for Advanced Simulation of Light Water Reactors

CIPS crud-induced power shift

CTF COBRA-TF

Hi2Lo high-to-low

HTC heat transfer coefficient

INL Idaho National Laboratory

KDE kernel density estimates

LHS Latin hypercube sample

MI mutual information

NMV non-mixing vane

ODE ordinary differential equations

PDE partial differential equations

PWR pressurized water reactor

QoI quantities of interest

SA sensitivity analysis

UQ uncertainty quantification

UO_2 uranium dioxide

WEC Westinghouse

(This page intentionally left blank)

Chapter 1

Introduction

The high-to-low (Hi2Lo) initiative in the Consortium for Advanced Simulation of Light Water Reactors (CASL) broadly focuses on the use of validated high-fidelity simulation codes to inform, improve and calibrate low-fidelity codes to facilitate multiphysics coupling, design, performance analysis, and risk assessment. The present emphasis has focused on the high-fidelity codes STAR-CCM+ and BISON and low-fidelity codes COBRA-TF (CTF), CTFFuel, and various associated closure relations. During the remainder of the program, this emphasis will be expanded to include MAMBA. Current CASL applications of Hi2Lo primarily use validated high-fidelity codes to simulate data for operating regimes in which experimental data is not available or prohibitively expensive to collect. However, the underlying experimental design is equally applicable to experimental data, and we additionally demonstrate the process using 5×5 non-mixing vane (NMV) data to calibrate the turbulent mixing coefficient β in the low-fidelity CTF.

The objectives of the CASL Hi2Lo analyses are multifold.

(i) Employ physics encapsulated in high-fidelity codes to improve the functionality of low-fidelity codes.

(ii) Quantify and incorporate biases or discrepancies in low-fidelity codes.

(iii) Develop and calibrate physical models and closure relations so that low-fidelity codes more accurately incorporate requisite physics. We demonstrate initial work focused on the Dittus–Boelter closure relation in CTF and a gas gap closure relation developed for CTFFuel. FY17 milestones focused significantly on the implementation and demonstration of the framework and development of appropriate fuel models. The use of the Hi2Lo framework to calibrate these models constitutes a significant effort for FY18.

(iv) Develop low-fidelity codes that can be effectively coupled to simulate multiphysics behavior. For example, one objective is to replace BISON by CTFFuel to provide the efficiency required for full-core simulations.

The Hi2Lo efforts are intended to impact both CIPS and DNB [19]. Due to the prohibitive computational expense of coupled STAR/MAMBA at the full-core simulation level, single-pin or simple reduced-rod bundle models, which are computationally feasible, will be used to develop STAR-informed CTF/MAMBA subchannel models for full-core simulation. Similarly, a major FY17 effort has focused on the implementation of appropriate fuel models so that coupled MPACT/CTFFuel can be used to adequately quantify grid spacer effects, gap thickness, and dynamic gap conductance effects to accurately model crud-induced power shift (CIPS). Similarly, quantification of how spacer grids act to enhance downstream heat transfer effects constitutes one component of DNB.

During FY17, several milestones – which we denote as Type 1 milestones – contributed directly to the Hi2Lo program. There were also two Type 2 milestones, which provided physical models, closure relations and CASL packages required for future Hi2Lo analysis in FY18.

Type 1 Miletones:

- L3:AMA.CP.P14.04 [6] – This collaborative milestone with Westinghouse focused on the use of STAR to improve the grid modeling capabilities of CTF. As summarized in Chapter 4, this included initial quantification of STAR uncertainties due to variability in employed turbulence models and STAR-motived improvements of directed cross-flow relations in CTF.
- L3:VVI.H2L.P15.01 [5] – As detailed in Chapter 3, the objective of this milestone was to demonstrate the implementation of the experimental design-based Hi2Lo framework in Dakota to calibrate the turbulent mixing coefficient β in CTF using both STAR simulations and 5×5 non-mixing vane experimental data. This employed the enhanced Dakota capabilities developed in L2:VVI.P15.04.
- L3:VVI.H2L.P15.02 [4] – This complemented L3:VVI.H2L.P15.01 and focused on initial uncertainty quantification (UQ) and validation of STAR using Westinghouse 5×5 non-mixing vane data, and the use of STAR to generate synthetic data to calibrate β in CTF.
- L3:VVI.DAK.P15.01 – This milestone focused on extending the capabilities of the experimental design framework, central to the Hi2Lo program, to accommodate the inherent correlation between inputs and predictions when calibrating low-fidelity codes and inherently high-dimensional parameter and prediction spaces [3, 15]. Aspects of this milestone also focused on the development of active subspace techniques required for future coupled code calibration [10]. This milestone also supported L3:AMA.CP.P14.04, L3:VVI.H2L.P15.01 and L3:VVI.H2L.P15.02.
- L2:VVI.P15.04 – This milestone supported the implementation of the experimental design framework and extensions of Bayesian calibration regimes required to autonomously implement the Hi2Lo framework in Dakota for VERA use. The implementation of this framework for STAR/CTF is demonstrated in Chapter 3 for the milestones L3:VVI.H2L.P15.01 and L3:VVI.H2L.P15.02.

Type 2 Milestones:

- L3:PHI.P15.01 [22] – As summarized in Chapter 5, this milestone focused on the implementation of fuel models and closure relations to extend the capabilities of CTFFuel. We provide initial calibration results in Section 2.4.2, and the complete calibration of these closure relations, using both experimental and BISON-generated synthetic data, constitutes a major Hi2Lo effort for FY18.
- L2:PHI.P15.04 [18] This milestone summarized the improvements and extensions made during FY17 to CTF. This included discussion of the Hi2Lo investigation focused on STAR-informed extensions to CTF. Without modification, CTF cannot quantify complex spatially-dependent heat transfer behavior, caused by mixing vane grids, due to its low spatial resolution, lack of advanced turbulence models, and crude representation of the model geometry. The investigation [19] detailed an approach for developing heat transfer coefficient (HTC) multiplier maps to reconstruct this grid-generated heat transfer behavior for a single rod. This procedure is extended in [18] to a more realistic rod-bundle geometry, which requires the development of a multiplier map for each pin in the 5×5 bundle. This objective is similar to that investigated in L3:AMA.CP.P14.04 in the sense that it focused on the high-fidelity code STAR to inform and improve the low-fidelity code CTF.

Chapter 2

Calibration, Validation, and Verification Framework for CASL High- and Low-Fidelity Codes

We depict in Figure 2.1 the hierarchy of high- and low-fidelity CASL codes and surrogate models and indicate the steps where calibration, validation and verification arise. The experimental design component, which is central to the Hi2Lo program, lies at the interface between the low-fidelity codes and high-fidelity codes or experimental data. We summarize aspects of the thermal-hydraulics and fuels codes to motivate issues that were investigated in FY17 and will be addressed in the FY18 program. Similar issues pertain to the chemistry and neutronics codes.

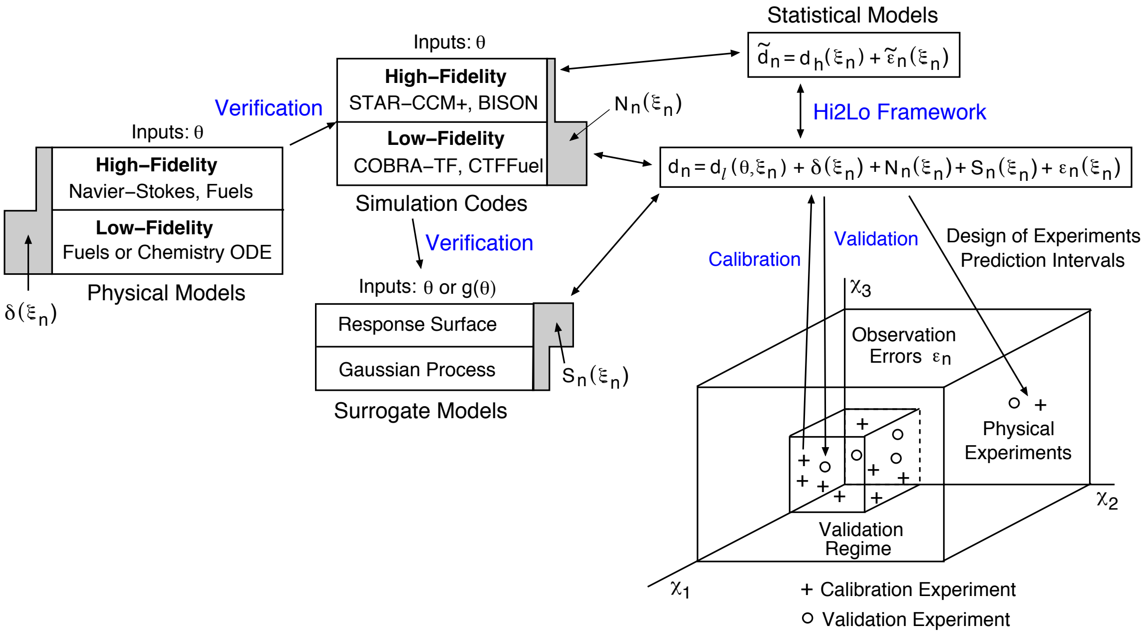

Figure 2.1. Hierarchy of CASL simulation codes, surrogate models, and calibration, validation, and verification framework.

2.1 CASL Codes

2.1.1 Thermal-Hydraulics Codes

In principle, computational fluid dynamics (CFD) codes such as STAR-CCM+, provide the capability to highly resolve fluid physics using techniques such as Reynolds averaging, large eddy simulations, various turbulence models, and even direct numerical simulations. However, the meshes required to resolve the physics precludes their use for full-core simulations or multiphysics packages such as TIAMAT. Furthermore, the use of CFD codes for two-phase flow modeling constitutes an active research area.

These limitations are addressed through the use of the subchannel code CTF. Whereas the STAR simulations for the geometry discussed in Chapter 3 require approximately 1000 core hours, the CTF simulations take approximately 5 minutes on a single processor (0.08 core hours). The ramification of this coarse meshing is the loss of fine-scale physics, which affects turbulent flow behavior, rod temperature profile and heat transfer, fluid mixing, and boundary layer behavior caused by features such as spacer grids. For example, the "wiping out" of spacer grid effects can yield average temperatures that are below local saturation temperatures thus affecting the predicted amount of crud deposited on rods. This demonstrates the necessity of quantifying spacer grid effects when analyzing crud-induced power shift (CIPS).

To address these limitations, several CASL initiatives have focused on the development of closure relations and model improvements in CTF to incorporate downstream grid effects [6, 18, 19]. One objective of the Hi2Lo program is to use STAR – augmented by experimental data when available – to improve the grid modeling capabilities of CTF and calibrate developed closure relations. The advantage of using a validated code, such as STAR, is that one can generate significant quantities of synthetic data for configurations where experimental data is unavailable.

As noted in the Introduction and detailed in Chapter 4, the AMA milestone L3:AMA.CP.P14.04 focused on initial quantification of uncertainties due to variability in employed turbulence models and STAR-motivated improvement of directed cross-flow relations in CTF. In combination, the milestones L3:VVI.H2L.P15.01 and L3:VVI.H2L.P15.02 demonstrated the implementation via Dakota of the experimental design-based Hi2Lo framework, summarized in Section 2.5, for using STAR to calibrate the turbulent mixing coefficient β in CTF.

FY18 milestones will focus on the use of STAR to create multipliers that can be applied to mixing coefficients in CTF to account for spacer grid enhanced turbulent mixing within subchannels. They will also focus the use of STAR to calibrate coefficients in the developed closure relations.

To employ STAR to calibrate CTF closure relations, it is necessary to ensure that the physics and design configurations are compatible. This includes the computed densities, specific heats and temperatures. Compatibility can entail both the solvers used in the two codes – equations of state or single versus two phase flows – and integrated versus nonintegrated temperatures. This is detailed in Section 3.2.3.

2.1.2 Fuels Codes

BISON is a finite-element nuclear performance code that can simulate temperature and burnup-dependent thermal properties, thermal and irradiation creep, fission product swelling, and fission gas production and release. However, its broad applicability renders it too computationally complex for full-core simulations when coupled in multiphysics packages such as TIAMAT. Moreover, BISON does not have the full physics required to quantify gaps between cladding and fuel.

As an alternative, significant effort has focused on the implementation of new fuel deformation models in the finite-difference package CTFFuel to make it viable for CASL multiphysics modeling. As detailed in [22] and Chapter 5, modeling implemented as part of the milestone L3:PHI.P15.01 included fuel swelling, fuel irradiation-induced densification, and fuel relocation.

To motivate aspects of the models developed in [22], we note that there are two options in CTF for computing the gas gap conductance: user-specified gas gap conductance in the radial and axial directions and a dynamic gas gap conductance model. In the dynamic gap conductance option, the gap conductance is given by

$$h_{gap} = h_{gas} + h_{rad} + h_{contact}, \tag{2.1}$$

where the gas conductivity in the gap h_{gas}, conductance to radiation h_{rad}, and solid-solid contact conductance $h_{contact}$, which incorporates potential physical contact between the fuel pellet and cladding, are given by

$$\begin{aligned} h_{gas} &= \frac{k_{gas}}{D_{mp} + (g_1 + g_2)} = \frac{k_{gas}}{\Delta t_{gap}} \\ h_{rad} &= \sigma_{SB} \frac{(T_f^4 - T_c^4)/(T_f - T_c)}{\frac{1}{\varepsilon_f} + \left(\frac{1}{\varepsilon_c} - 1\right)\frac{A_f}{A_c}} \\ h_{contact} &= C k_m F(L_i, R_i) \left(\frac{P_{int}}{H}\right)^n . \end{aligned} \tag{2.2}$$

Here σ_{SB} denotes the Stefan-Boltzmann constant, T_f, T_c are the fuel surface and clad inside temperatures, A_f, A_c are corresponding areas, ε is the surface emissivity, C is an empirical correlation, and P_{int} is the interfacial pressure. Furthermore, H denotes the Meyer hardness, k is the thermal conductivity, D_{mp} denotes the mean width between the fuel and cladding, $(g_1 + g_2)$ is the temperature jump distance, and Δt_{gap} denotes the gap thickness. In the last relation, $F(L_i, R_i)$ is a function of the peak-to-peak asperity separation L_i and the surface roughness R_i. We note that Δt_{gap} depends on closure relations for $(g_1 + g_2)$ and hence must be calibrated for considered operating regimes.

The gap thickness was originally computed in CTF by accounting for the fuel pellet/clad thermal expansions and cladding elastic deformations. However, there are additional fuel and cladding deformation physics that must be incorporated. The computation of the gap conductance is complicated by the difficulty of measuring the gap thickness and conductance through the reactor's life; note that the gap thickness is ~ 100 microns at the beginning of the reactor's life and approaches zero when the gap is closed.

We illustrate in Section 2.4.2 initial calibration of the static gas gap conductance model using BISON-generated data. We summarize in Chapter 5 the fuel swelling, fuel irradiation-induced densification, and fuel relocation models developed in [22] to incorporate dynamic behavior and missing physics. We also summarize how the Hi2Lo framework will be employed to calibrate model parameters in FY18 milestones.

2.2 Statistical Models for High- and Low-Fidelity Codes

The high-fidelity codes STAR and BISON and low-fidelity codes CTF and CTFFuel quantify the physics associated with thermal-hydraulics and fuels. To provide a rigorous framework for calibration and experimental design, it is necessary to additionally formulate statistical models that quantify the observation process associated with high and low-fidelity models. The relation of these statistical models to the physical simulation codes and experimental data is depicted in Figure 2.1.

We let $d_\ell(\theta, \xi_n)$ denote the low-fidelity model, which could be CTF, closure relations in CTFFuel, or closure relations in other CASL codes. Here $\theta = [\theta_1, \ldots, \theta_p]$ denotes parameters that we seek to calibrate using either synthetic data constructed using a high-fidelity code or experimental data. In Chapter 3, we demonstrate the calibration of the turbulence mixing coefficient $\theta = \beta$ in CTF whereas in Section 2.4.2, θ are parameters in a gap conductance closure relation. We let ξ_n denote design or configuration conditions. For the examples in Chapter 3, these include the exit pressure, inlet temperature, inlet mass flow rate, and average linear heat rate per rod. Low-fidelity observations d_n are then given by the statistical model

$$d_n = d_\ell(\theta, \xi_n) + \delta(\xi_n) + N_n(\xi_n) + S_n(\xi_n) + \varepsilon_n(\xi_n), \tag{2.3}$$

where we denote potential additive discrepancy or biases in the low-fidelity model by $\delta(\xi_n)$ and random observation or discretization errors by $\varepsilon_n(\xi_n)$. Potential numerical errors resulting from the discretization of governing ordinary differential equations (ODE) or partial differential equations (PDE) are denoted by $N_n(\xi_n)$ whereas surrogate model errors are given by $S_n(\xi_n)$.

For a given design ξ_n, the n^{th} observation $\tilde{d}_n$, generated by the high-fidelity model $d_h(\xi_n)$, is given by

$$\tilde{d}_n = d_h(\xi_n) + \tilde{\varepsilon}_n(\xi_n). \tag{2.4}$$

Here $\tilde{\varepsilon}_n(\xi_n)$ denotes additive observation uncertainties or errors. Whereas one often assumes that these uncertainties are independent and identically distributed (iid) and normally distributed with variance $\tilde{\sigma}^2$, that is $\tilde{\varepsilon}_n(\xi_n) \overset{iid}{\sim} N(0, \tilde{\sigma}^2)$, this will likely not be the case for STAR and, in some cases, one may have only bounds for errors.

2.3 Validation and Verification Frameworks

The discretization of governing PDE, ODE and algebraic closure relations yields numerical errors, which we denoted in Figure 2.1 by $N_n(\xi_n)$. These errors are mesh-dependent and may vary in codes, such as STAR, when different meshes are employed among various groups. We do not focus directly in the Hi2Lo program on the verification step of quantifying these errors but note that they can affect calibration and uncertainty analysis. Hence, when available, we do incorporate them into the statistical models (2.3) and (2.4).

Similarly, the use of surrogate models introduces errors, which we denote by $S_n(\xi_n)$ in Figure 2.1 and (2.3). As we demonstrate in Chapter 3, verification constitutes a fundamental step when constructing surrogate models for use in Hi2Lo-based model calibration.

Full-scale validation of high- and low-fidelity codes generally lies beyond the scope of CASL. For Hi2Lo and uncertainty analysis, however, one needs to ascertain potential model discrepancies or biases $\delta(\xi_n)$. Furthermore, the validity of employing high-fidelity codes to generate synthetic data for subsequent calibration is predicated on the assumption that they are employed in regimes where they have been validated. Hence as part of the Hi2Lo demonstration in Chapter 3, we include initial validation results for STAR in the regime used to calibrate β in CTF. We emphasize that some form of validation is necessary when employing high-fidelity codes to generate data for low-fidelity model improvement or calibration.

2.4 Calibration Framework

A primary function of the Hi2Lo framework is to calibrate parameters $\theta = [\theta_1, \ldots, \theta_p]$ in the statistical model (2.3) for low-fidelity models and closure relations. One can obtain point estimates by employing optimization routines in Dakota. However, these estimates do not quantify parameter uncertainties due to observation errors $\varepsilon_n(\xi_n)$, model biases $\delta(\xi_n)$ or numerical errors $N_n(\xi_n)$ and $S_n(\xi_n)$. To incorporate these uncertainties, we employ a Bayesian framework in the manner detailed in [1, 20].

The basis for this framework is Bayes relation

$$\pi(\theta|\tilde{d}_n) = \frac{\pi(\tilde{d}_n|\theta)p(\theta)}{\int_{\mathbb{R}^p} \pi(\tilde{d}_n|\theta)p(\theta)d\theta}, \tag{2.5}$$

where $p(\theta)$ denotes the prior distribution, $\pi(\tilde{d}_n|\theta)$ is the likelihood which combines information provided by the model and data, and $\pi(\theta|\tilde{d}_n)$ denotes the posterior distribution. Here $\tilde{d}_n$ denotes either synthetic data from a validated high-fidelity code, with the associated statistical model (2.4), or experimental data. To illustrate a common choice for the likelihood, we consider the simplified statistical model

$$\tilde{d}_n = d_\ell(\theta, \xi_n) + \varepsilon_n(\xi_n)\ ,\ \ n = 1, \ldots, N \tag{2.6}$$

for the low-fidelity model $d_\ell(\theta, \xi_n)$; e.g., compare to (2.3) with the assumption of negligible model discrepancies $\delta(\xi_n)$ and numerical errors $N_n(\xi_n), S_n(\xi_n)$. If the observations errors $\varepsilon_n(\xi_n)$ are assumed to be independent and identically distributed (iid) and normally distributed with variance σ^2; i.e., $\varepsilon_n(\xi_n) \overset{iid}{\sim} N(0, \sigma^2)$, the likelihood is

$$\pi(\tilde{d}_n|\theta) = \frac{1}{(2\pi\sigma^2)^{N/2}} e^{-\sum_{n=1}^{N} \left[\tilde{d}_n - d_\ell(\theta,\xi_n)\right]^2/2\sigma^2}. \tag{2.7}$$

We note that the assumption $\varepsilon_n(\xi_n) \overset{iid}{\sim} N(0, \sigma^2)$ is often violated, which can require the consideration of more general likelihood relations. Moreover, when employing either synthetic high-fidelity data, or experimental data, it is necessary to quantify the observation errors $\tilde{\varepsilon}_n(\xi_n)$ in (2.4) in some manner.

When possible, we directly calibrate and perform uncertainty quantification (UQ) for the low-fidelity CASL code of interest. For some cases, however, it is first necessary to construct and verify a surrogate model for the code in the manner detailed in Chapter 4 of [1]. We re-address the use of surrogate models in Section 2.5 when we discuss mutual information-based experimental design. Finally, we note that highly efficient Bayesian inference on active parameter subspaces for CASL applications is detailed in [10].

We next illustrate this calibration framework for the Dittus–Boelter closure relation in CTF and a gap conductance closure relation.

2.4.1 Calibration of the Dittus–Boelter Relation and Uncertainty Propagation through CTF

To demonstrate the Bayesian calibration framework in Dakota and the role of inverse and forward uncertainty quantification techniques, we considered the Dittus–Boelter closure relation

$$Nu = \theta_1 Re^{\theta_2} Pr^{\theta_3} \tag{2.8}$$

employed in CTF. Here Nu, Re and Pr respectively denote the Nusselt, Reynolds, and Prandtl numbers and $\theta = [\theta_1, \theta_2, \theta_3]$ are model parameters. For single-phase flows in round, smooth, pipes, these parameters have the nominal values $\theta_1 = 0.023, \theta_2 = 0.8$ and $\theta_3 = 0.4$. For two-phase flows and more general operating regimes, however, there are no established values for the parameters so we employ Bayesian inference, summarized in Section 2.4, to infer distributions and associated mean values using experimental data.

For the Dittus–Boelter model (2.8), a common industry standard is to ensure that parameters are positive and bounded by twice the nominal values. Hence we employ a uniform prior distribution on the intervals

$$\theta_1 \in [0, 0.046]\ ,\ \theta_2 \in [0, 1.6]\ ,\ \theta_3 \in [0, 0.8]. \tag{2.9}$$

Using this prior distribution and experimental data from [16], we employed a Delayed Rejection Adaptive Metropolis (DRAM) algorithm [7] to infer the marginal posterior densities plotted in Figure 2.2 and pairwise distributions plotted in Figure 2.3. From the former, we note that 2σ is approximately $0.0035, 0.06$ and 0.03 for the three parameters. Hence we have significantly reduced the uncertainty as compared with the conservative bounds in (2.9). Furthermore, Figure 2.3 demonstrates that we are additionally quantifying the correlation inherent to the three parameters, which is not accommodated by a uniform distribution on the region $[0, 0.046] \times [0, 1.6] \times [0, 0.8]$.

We then propagated samples from the uniform prior distribution on $[0, 0.046] \times [0, 1.6] \times [0, 0.8]$, the marginal posterior distributions plotted in Figure 2.2, and the joint posterior distribution incorporating the correlation shown in Figure 2.3 through CTF to compute the maximum fuel temperature distributions plotted in Figure 2.4. The first two cases exhibit variability on the order of 40^o whereas use of the joint distribution reduces this variability to approximately 10^o. This demonstrates the manner in which Bayesian model calibration followed by uncertainty propagation can significantly reduce uncertainties in CASL quantities of interest (QoI).

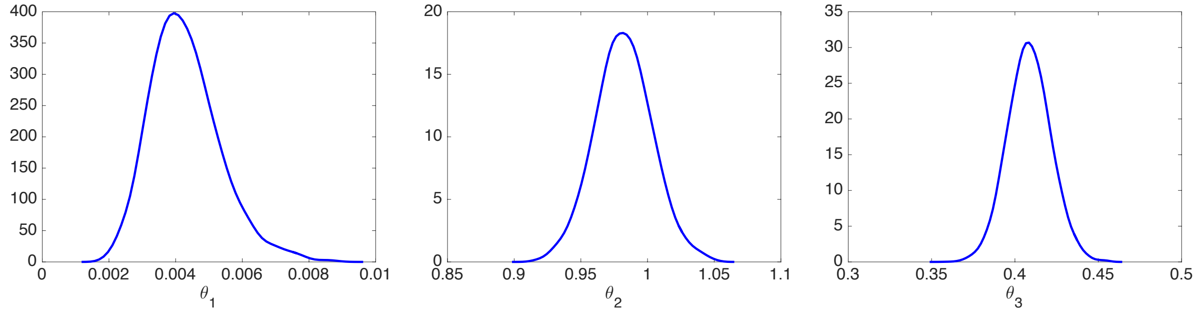

Figure 2.2. Marginal densities for θ_1, θ_2 and θ_3.

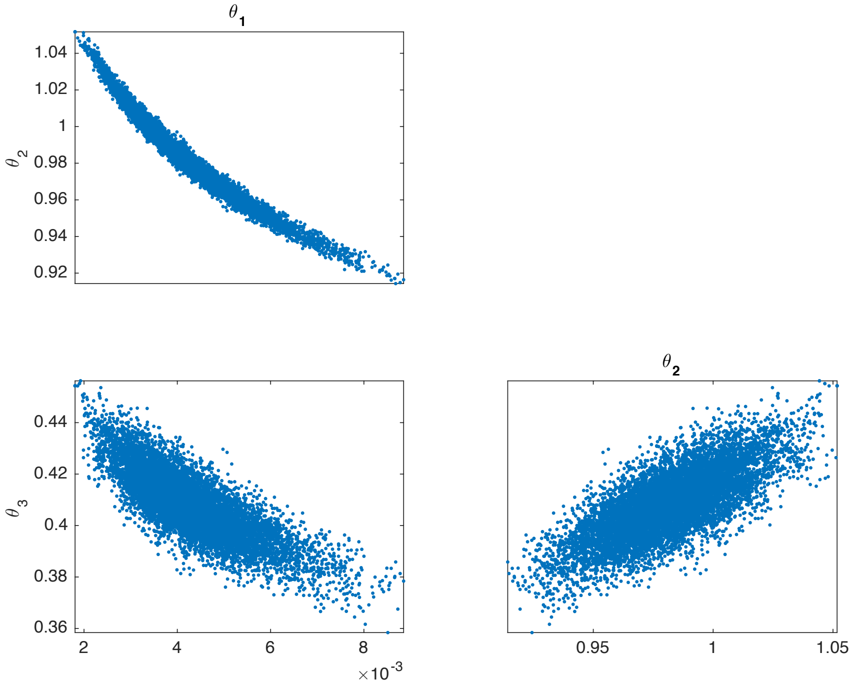

Figure 2.3. Pairwise distributions for θ_1, θ_2 and θ_3.

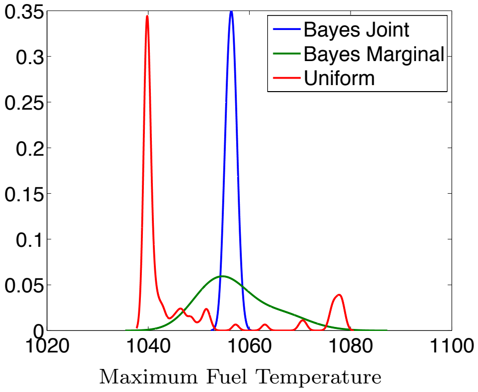

Figure 2.4. Uncertainty in maximum fuel temperature.

2.4.2 Calibration of a Gap Conductance Closure Relation

As a first step toward the development of closure relations for CTFFuel in L3:PHI.P15.01, the authors of [22] developed and calibrated an initial closure relation for the gas gap thickness Δt_{gap} in (2.2). BISON simulations were run for a single pellet of a standard pressurized water reactor (PWR) uranium dioxide (UO_2) fuel for a power rate of 18.383 kW/m. The gap conductance through depletion is plotted in Figure 2.5. Figure 2.6 demonstrates the BISON simulations for linear rates ranging from 1.0 to 40.0 kW/m and clad outside temperatures from 475 to 625 K.

These high-fidelity simulations were then used to infer distributions for the parameters $\theta = [\theta_1, \ldots, \theta_6]$ in the gas gap thickness relation

$$\frac{\Delta t_{gap}}{t_{gap}} = \theta_1 T_{ci} + \left[\theta_2 q'^3 + \theta_3 q'^2 + \theta_4 q' + \theta_5\right] + \theta_6 Bu, \tag{2.10}$$

using the Bayesian model calibration framework summarized in Section 2.4. Here T_{ci} denotes the cladding inside temperature (K), q' is the linear power rate (W/m), and Bu is the burnup (MWd/MTU).

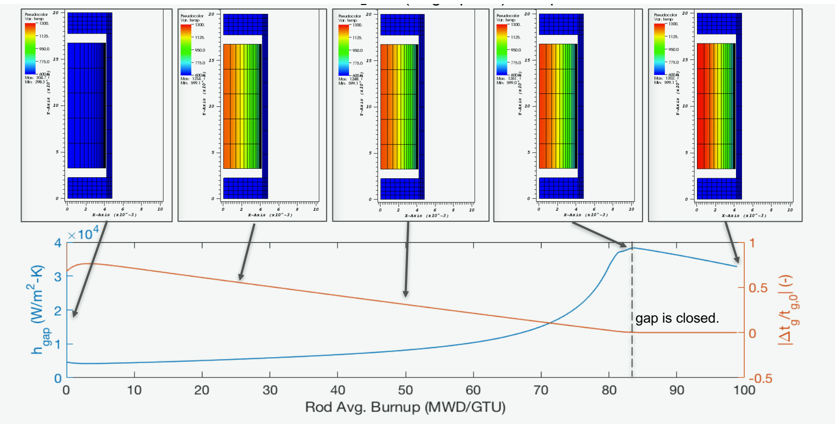

Figure 2.5. BISON simulation results for a standard PWR single pellet UO_2 for a power rate of 18.383 kW/m.

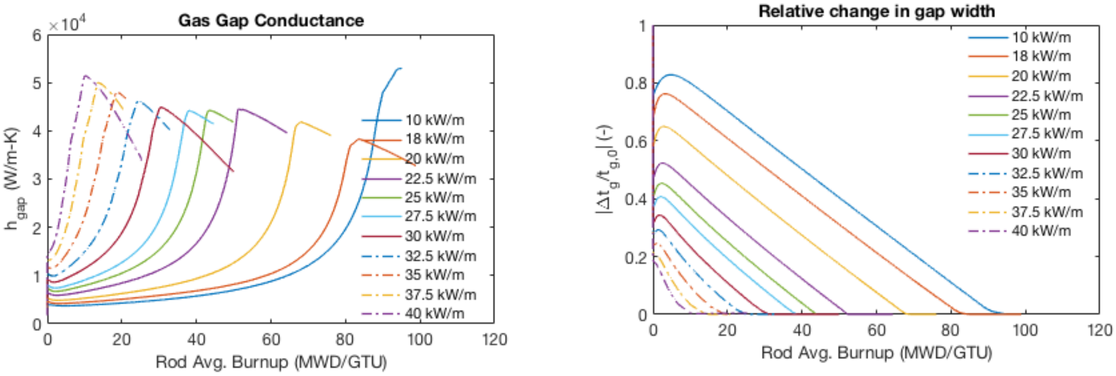

(a) (b)

Figure 2.6. BISON simulated data for (a) gas gap conductance and (b) relative change in gap width.

The mean parameter values provided by DRAM [7] are compared with the point estimates obtained through optimization in Table 2.1 and the pairwise posterior parameter distributions are plotted in Figure 2.7. Whereas the mean parameter values closely correspond to the optimal values, Bayesian inference additionally quantifies inherent correlation between parameters such as that observed between (θ_2, θ_3) and (θ_2, θ_4).

The relation (2.10) might not provide accurate predictions of transient thermal-mechanical behavior of the fuel rod and does not account for transient dynamics. Hence it does not have the capability to model transient changes in the gap thickness and conductance as required for CASL challenge problems. As detailed in [22], CTFFuel quantifies these dynamic effects. Hence a significant component of the FY18 program will focus the use of the Hi2Lo framework to calibrate parameters in CTFFuel closure relations.

	Initial Values	Optimal Values	Mean Values
θ_1	-3.59×10^{-4}	-4.31×10^{-4}	-3.23×10^{-4}
θ_2	-3.58×10^{-14}	3.80×10^{-14}	4.16×10^{-14}
θ_3	-2.52×10^{-9}	-2.63×10^{-9}	-2.88×10^{-9}
θ_4	2.77×10^{-5}	2.64×10^{-5}	3.16×10^{-5}
θ_5	0.82	1.18	1.09
θ_6	1.00	-0.01	-0.01

Table 2.1. Initial, optimized and mean parameter values obtained using DRAM.

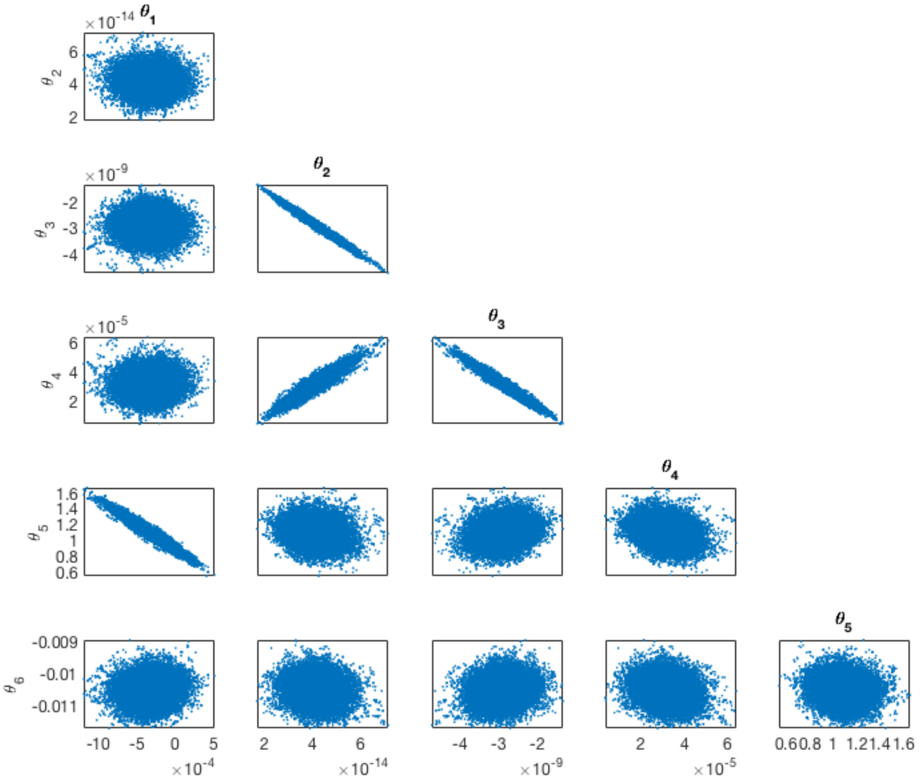

Figure 2.7. Pairwise distributions for $\theta_1, \ldots, \theta_6$.

2.5 Mutual Information-Based Experimental Design

As noted previously, the computational cost of STAR and BISON simulations to generate data precludes comprehensive coverage of the complete design space. Furthermore, their computational complexity prohibits their use in coupled multi-physics packages, such as TIAMAT, for performing full-core simulations. Here we summarize the use of mutual information-based experimental design [2, 11, 12, 21] to specify where in the design space to run high-fidelity codes – e.g., STAR or BISON – to optimally inform parameters in the low-fidelity code – e.g., β in CTF.

Given a set of observations $D_{n-1} = \{\tilde{d}_1, \tilde{d}_2, ..., \tilde{d}_{n-1}\}$ of the high-fidelity code, we seek a design or evaluation strategy $\xi_n \in \Xi$ so that uncertainty in low-fidelity model parameters $\theta \in \mathbb{R}^p$ is reduced when the model is re-calibrated using the new high-fidelity data point $\tilde{d}_n$. Here Ξ designates the set of possible evaluation strategies or experimental conditions.

The change in knowledge about the model parameters, due to the addition of new synthetic or experimental data $\tilde{d}_n$, is given by Bayes' rule

$$p(\theta|D_n) = \frac{p(D_n|\theta)p(\theta)}{p(D_n)} = \frac{p(\tilde{d}_n, D_{n-1}|\theta)p(\theta)}{p(\tilde{d}_n, D_{n-1})}$$

for the new data set $D_n = \{\tilde{d}_n, D_{n-1}\}$. The goal in experimental design is to optimize the information provided by an experiment or high-fidelity observation $\tilde{d}_n$ based on the design ξ_n. Because our objective is to determine the distribution of the model parameters θ from the calibration of our low-fidelity model with data $\tilde{d}_n$, using as few experiments as possible, the strategy upon which we base our design decision should be chosen according to the amount of information provided by the proposed data as a result of measuring under design conditions ξ_n. Since $\tilde{d}_n$ has not yet been observed when we make a decision regarding the choice of ξ_n, we employ predictions d_n provided by the statistical model (2.3) to determine ξ_n.

As detailed in [11], the optimal design ξ_n^* maximizes the mutual information

$$I(\theta; d_n|D_{n-1}, \xi_n) = \int_{\mathcal{D}} \int_{\Omega} p(\theta, d_n|D_{n-1}, \xi_n) \log \frac{p(\theta, d_n|D_{n-1}, \xi_n)}{p(\theta|D_{n-1})p(d_n|D_{n-1}, \xi_n)} d\theta dd_n; \tag{2.11}$$

that is,

$$\xi_n^* = \arg \max_{\xi_n \in \Xi} I(\theta; d_n|D_{n-1}, \xi_n). \tag{2.12}$$

The high-fidelity code is then evaluated using the design condition ξ_n^* and the data $\tilde{d}_n$ resulting from statistical model (2.4) is used to recalibrate the model parameters θ.

The use of kNN (k^{th}-Nearest Neighbor) techniques to approximate the integrals in (2.11) is detailed in [9, 11] and the design implementation is summarized in Algorithm 1. The extension of the algorithm to accommodate inherent correlation between low-fidelity model parameters and predictions and high dimensional parameter and prediction spaces was addressed in the milestone L3:VVI.DAK.P15.01 and is detailed in the report [15]. The implementation of the framework to calibrate β in CTF, using both STAR simulations and experimental 5×5 non-mixing vane data was addressed in L3:VVI.H2L.P15.01 and L3:VVI.H2L.P15.02 and is illustrated in Chapter 3. This includes the construction of a highly efficient surrogate model for CTF to facilitate both mutual information-based experimental design and Bayesian inference. The extensions to Dakota to facilitate autonomous implementation of the framework are detailed in L2:VVI.P15.04.

Algorithm 1 Design Implementation

```
(1) Define $N$, the number of samples to be used in the $k$NN algorithm.
(2) Initialize a list of pre-existing high-fidelity data, $D_r = [(\xi_1, \tilde{d}_1), (\xi_2, \tilde{d}_2), ..., (\xi_r, \tilde{d}_r)]$.
(3) Define the list of possible design conditions, $\Xi = [\xi_{r+1}, \xi_{r+2}, ..., \xi_s]$.
(4) If $r \geq 1$, run the Dakota-QUESO DRAM algorithm to construct a chain $\{\theta^i\}_{i=1}^N$ of size $p \times N$ from the prior distribution $p(\theta|D_r)$, where $p$ is the number of parameters. If $r = 0$; that is, there are no pre-existing data, construct a chain of size $p \times N$ by sampling a proper prior $p(\theta)$ of choice.
(5) Send the chain $\{\theta^i\}$ and corresponding synthetic data simulated from (2.3) to the $k$NN algorithm.
(6) The $k$NN algorithm returns a single design condition $\xi_n \in \Xi$. Append this value and the corresponding high-fidelity prediction $\tilde{d}_n$ from (2.4) evaluated at $\xi_n$ to the previous data list to obtain
        $D_{r+1} = [(\xi_1, \tilde{d}_1), (\xi_2, \tilde{d}_2), ..., (\xi_r, \tilde{d}_r), (\xi_n, \tilde{d}_n)]\,.$
(7) Set $r = r + 1$ and repeat steps 3-6 until all designs are used or a user-specified error tolerance is met.
```

Chapter 3

Demonstration of Hi2Lo Framework for STAR/CTF

A primary function of the Hi2Lo framework is to employ synthetic data generated using validated high-fidelity codes to calibrate closure relations or tuning parameters in low-fidelity codes in regimes for which experimental data is unavailable. The framework employs the mutual information-based experimental design framework, summarized in Section 2.5, to determine where in the design space to evaluate high-fidelity codes to gain the most information when calibrating parameters. We note that while the program focuses primarily on synthetic data generated using high-fidelity codes, the framework is equally applicable to experimental data.

In this chapter, we summarize the results of the milestones L3:VVI.H2L.P15.01 and L3:VVI.H2L.P15.02, which demonstrated the Hi2Lo framework to calibrate the turbulent mixing parameter β using both STAR-generated data and experimental data from Westinghouse. Since CTF does not have a turbulence model, β is tuned to accommodate, to the degree possible, turbulence effects incorporated in STAR and observed in experimental data. The statistical and VVUQ components of the Hi2Lo framework were implemented using Dakota version 6.6, as documented in the report for the milestone L2:VVI.P15.03.

We summarize the initialization, calibration and design steps from Algorithm 1 in Figure 3.1 and provide the milestone tasks and workflow in Figure 3.2. We summarize primary steps in this chapter and note that details regarding the complete process are provided in [4,5].

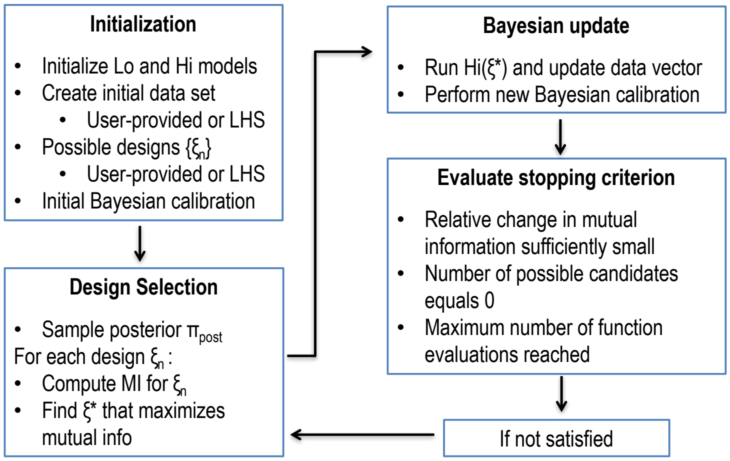

Figure 3.1. Initialization, calibration, and design steps in the mutual information-based experimental design framework.

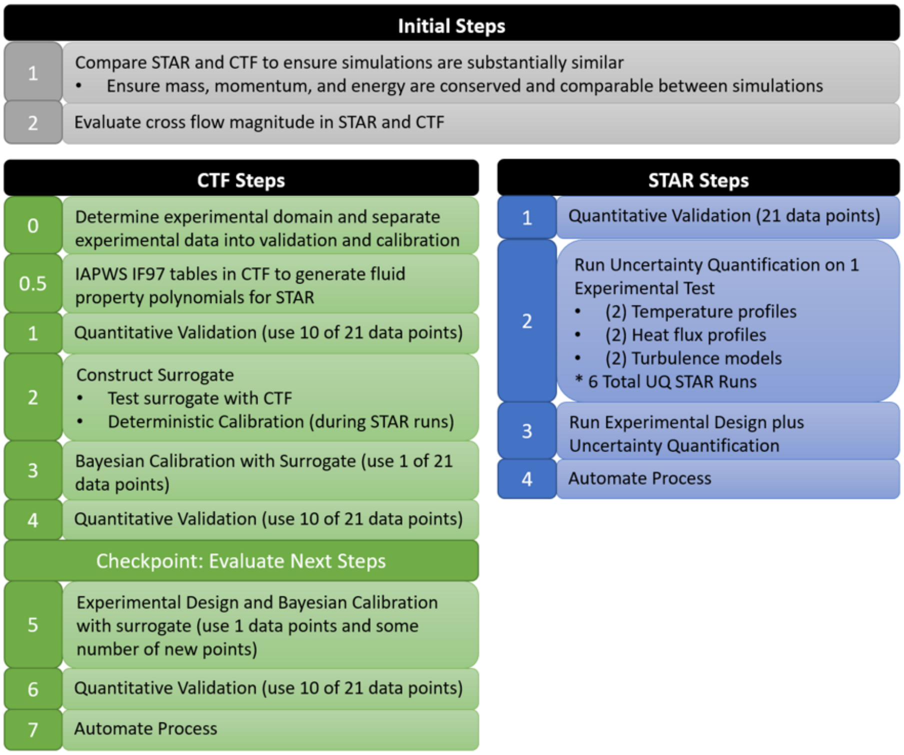

Initial Steps

1 Compare STAR and CTF to ensure simulations are substantially similar
  - Ensure mass, momentum, and energy are conserved and comparable between simulations

2 Evaluate cross flow magnitude in STAR and CTF

CTF Steps

0 Determine experimental domain and separate experimental data into validation and calibration

0.5 IAPWS IF97 tables in CTF to generate fluid property polynomials for STAR

1 Quantitative Validation (use 10 of 21 data points)

2 Construct Surrogate
  - Test surrogate with CTF
  - Deterministic Calibration (during STAR runs)

3 Bayesian Calibration with Surrogate (use 1 of 21 data points)

4 Quantitative Validation (use 10 of 21 data points)

Checkpoint: Evaluate Next Steps

5 Experimental Design and Bayesian Calibration with surrogate (use 1 data points and some number of new points)

6 Quantitative Validation (use 10 of 21 data points)

7 Automate Process

STAR Steps

1 Quantitative Validation (21 data points)

2 Run Uncertainty Quantification on 1 Experimental Test
  - (2) Temperature profiles
  - (2) Heat flux profiles
  - (2) Turbulence models

  * 6 Total UQ STAR Runs

3 Run Experimental Design plus Uncertainty Quantification

4 Automate Process

Figure 3.2. Milestones and workflow for the Hi2Lo framework.

3.1 WEC Experimental Data

Throughout this analysis, we employed data from Westinghouse (WEC) NMV grid, single bundle experiments. The axial geometry and location of grid spacers are depicted in Figure 3.3(a). Figure 3.3(b) displays a cross-section of the rod bundle used during the experiments. The bundle is comprised of 5 NMV grids in the heated length with 36 subchannels and 25 rods in a 5 × 5 array. The 6 rods highlighted in red in Figure 3.3(b) are the hot rods. All of the rods are electrically heated, but the hot rods have a higher power than the other rods.

Data from 23 experiments was provided by WEC with 2 omitted from the Hi2Lo analysis to ensure that test cases remain single phase. Based on input from Westinghouse, a repeatability error of $\pm 6^o$F (3.333^oC) was considered for the experimental data in addition to an uncertain amount of experimental error. Finally, we note that the Westinghouse test data are proprietary and were provided for CASL use under the proper Nondisclosure Agreement (NDA).

We employed all 21 tests when validating STAR. For CTF, 10 of the experiments were used for validation and 11 for calibration.

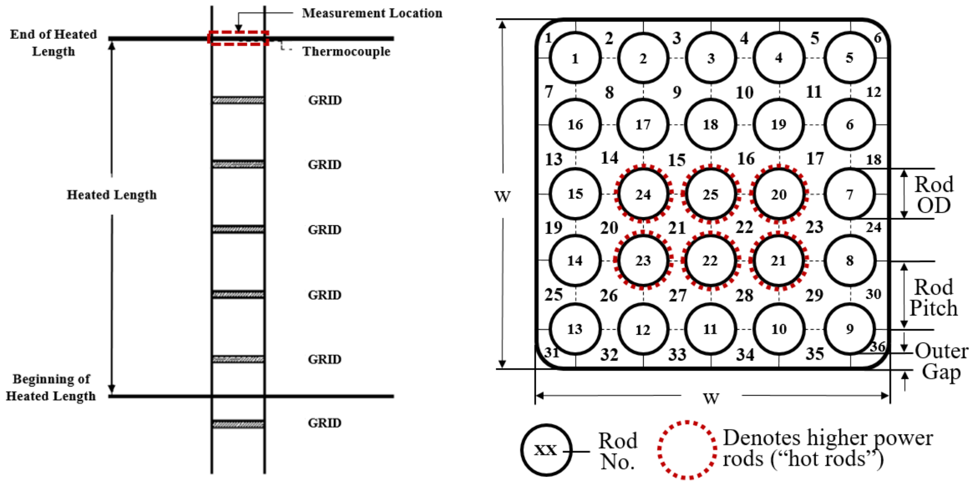

(a) (b)

Figure 3.3. (a) Axial view of experimental geometry and (b) cross-section of WEC NMV experiments.

3.2 STAR Validation and Calculations

As detailed in [4], there were four primary tasks pertaining to STAR: (i) validation, (ii) uncertainty and sensitivity analysis and initial determination of the observation errors $\tilde{\varepsilon}(\xi_n)$ depicted in Figure 2.1 and included in the high-fidelity model (2.4), (iii) use of CTF to generate functions to define STAR fluid properties, and (iv) computation of synthetic data to calibrate β in CTF. STAR simulations were run on Falcon at Idaho National Laboratory (INL) and each simulation required approximately 1000 core hours.

3.2.1 STAR Validation

As a first validation step, it was determined that STAR is correctly conserving mass, momentum and energy. While this seems apparent, it verifies that the code is correctly configured for the considered simulation regimes.

As a quantitative validation step, both STAR and CTF simulated temperatures were compared to the WEC data summarized in the last section. Qualitative comparison of the predicted STAR simulations and experimental data are provided in Figure 3.4 whereas quantitative comparisons, based on L_2 norms are provided in [4].

In this analysis, it was observed that the channel center temperature measurements have a lower L_2 norm value than the channel average temperatures, which was anticipated since the channel center temperatures – collected by probes at the center of the channels – more closely approximate the experimental data locations. This is relevant when using STAR to generate synthetic data to calibrate CTF. Moreover, the STAR simulations are symmetric whereas asymmetries are noted in the experimental data. As discussed in Section 3.3.3, this is important when explaining differences between β calibrated using STAR versus experimental data.

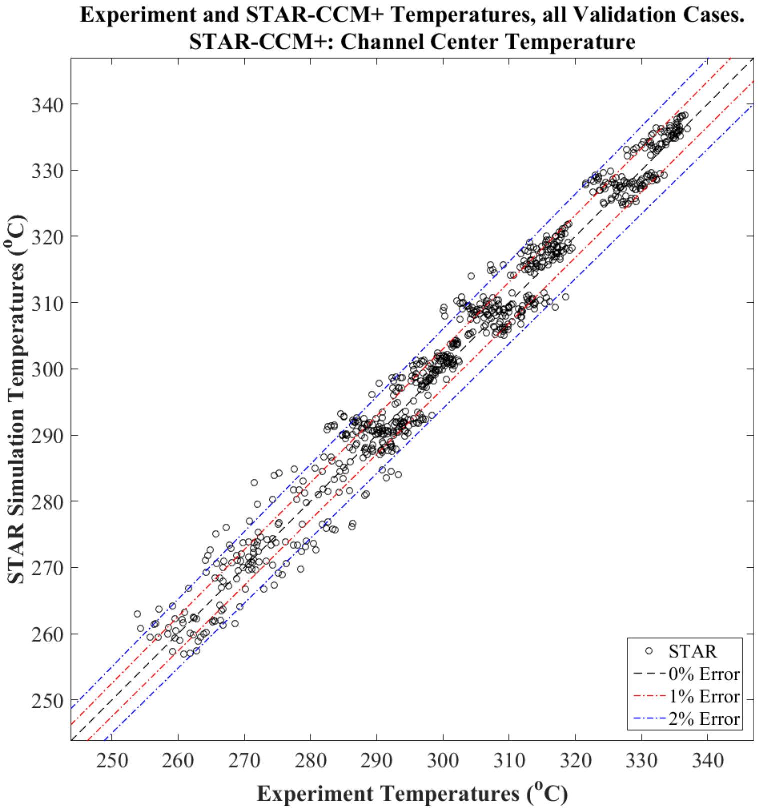

Figure 3.4. Experimental and STAR center temperatures.

3.2.2 Uncertainty and Sensitivity Analysis

As an initial step to quantify the observation errors $\tilde{\varepsilon}(\xi_n)$ and construct a high-fidelity statistical model (2.4) for STAR, uncertainty and sensitivity analysis (SA) was performed on STAR using the experimental conditions of Case 1 as inputs. For this analysis, the standard $k-\omega$ and realizable $k-\varepsilon$ turbulence models were considered in addition to two mass flow rate profiles and two total power distribution profiles. The resulting temperatures at the 36 subchannels for each of these 6 cases are plotted in Figure 3.5. Among the six considered parameter perturbations, the change from the $k-\omega$ turbulence model to the $k-\varepsilon$ model had the largest impact on the subchannel temperature. This should be considered an initial UQ/SA test leading to more detailed future investigations.

As a second step to quantify $\tilde{\varepsilon}(\xi_n)$ and construct an appropriate statistical model, we employed the experimental uncertainties of $\pm 3.333^o$C, reported by Westinghouse, to construct appropriate covariance matrices for STAR simulations. Details are provided in [5].

3.2.3 Generating Polynomials for STAR Inlet Fluid Conditions

To ensure that STAR and CTF are operating at the same fluid conditions throughout this process, CTF fluid properties were used to generate functions to define STAR fluid properties. STAR uses polynomial functions that are fit to fluid property data. To establish that CTF and STAR use the same fluid properties, polynomials were generated from CTF fluid property outputs. The properties needed to fully define the fluid in STAR include density, specific heat, thermal conductivity, and dynamic viscosity. Fluid properties were evaluated over a pressure range of 158 bar to 167 bar, representing 1% less than the minimum exit pressure and 1% more than the maximum inlet pressure respectively to ensure there is no extrapolation outside of the observed range. The resulting polynomials are reported in [5].

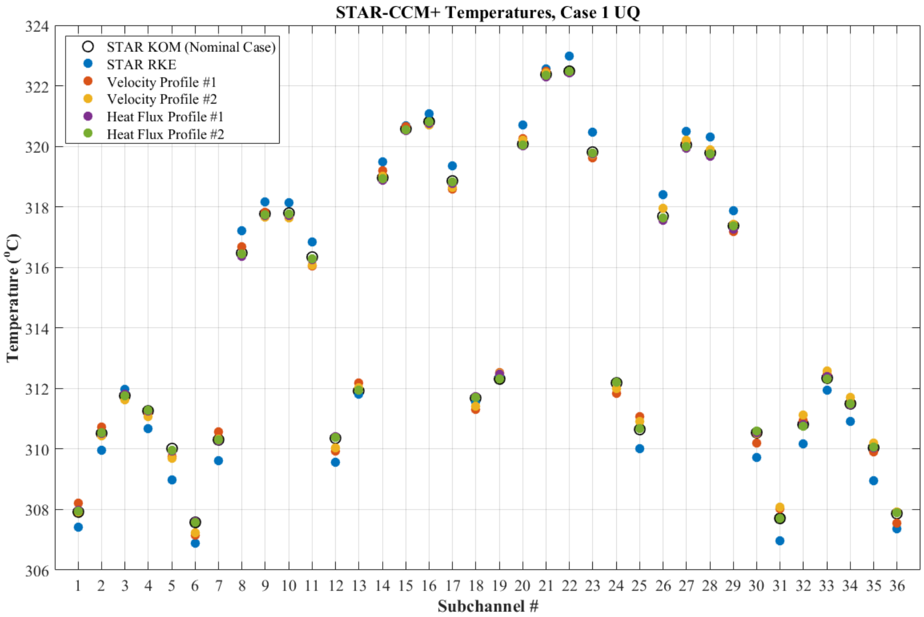

Figure 3.5. Perturbation results demonstrating that changing turbulence models most significantly affected temperatures.

3.2.4 Generation of Synthetic Data to Calibrate β in CTF

The experimental design in Dakota uses a list of candidate evaluation points, the Latin hypercube sample (LHS) design used in Bayesian calibration of CTF, and a calibration data file. The experimental design process was performed twice. The first experimental design used experimental conditions/results – only one test was used in the original calibration – as design points/ high-fidelity results. The second experimental design used STAR simulation conditions/results corresponding to the experimental evaluation points. The results of the two experimental design studies were compared once the entire experimental design procedure was complete.

This information was passed to Dakota using a manual process. The capability to perform the process inline with Dakota is possible with Dakota 6.6; however, we were not able to run CTF and STAR on the same computing resources. Once the high-fidelity simulation completes, results are passed back to Dakota. Additional configuration variables and their corresponding temperature results are supplied to Dakota as experimental design points.

3.3 Calibration and Validation of CTF

Here we summarize the steps required to implement the Hi2Lo framework to calibrate β in CTF using both STAR-generated synthetic data and experimental WEC data. In the notation of Chapter 2, the calibration parameter is $\theta = \beta$. The design or configuration variables ξ_n are the exit pressure, inlet temperature, inlet mass flow rate, and average linear heat rate per rod. The quantity of interest (QoI) throughout this analysis is the subchannel average outlet temperature.

Some key assumptions, which are made with the CTF analysis, are that the results are at steady-state and that no additional cross-flow effect modeling is needed. CTF is also a two-phase, compressible code; however, since the flow parameters configure the STAR and CTF simulations in the single-phase regime, it can be assumed that CTF behaves similarly to the single-phase, polynomial density STAR model. The NMV CTF model input deck uses symmetric input parameters, which results in symmetric flow.

In subsequent subsections, we detail the CTF Steps in Figure 3.1.

3.3.1 Initial Quantitative Validation of CTF

To ascertain improvements to CTF predictions that we anticipate when calibrating β, we performed initial validation using $\beta = 0$, which models the case of no mixing between subchannels in the bundle. The resulting CTF predictions are compared with the experimental data in Figure 3.6. Quantitative results in [5] indicate that statistically, the CTF outlet temperatures differ from experimental outlet temperatures by approximately 1.44%. This indicates that calibration of β can yield small but not profound improvements.

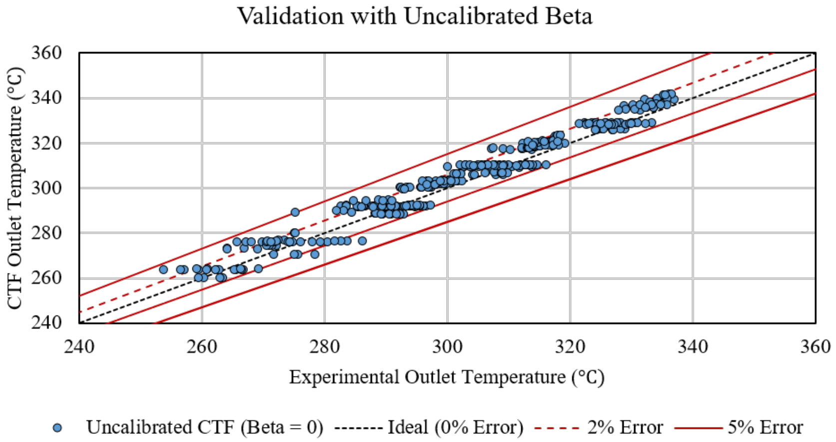

Figure 3.6. Validation results comparing CTF outlet temperatures computed with $\beta = 0$ and experimental outlet temperatures.

3.3.2 Surrogate Model Construction

For the considered geometry and conditions, CTF required approximately 5 minutes to run. Whereas significantly less than the hour required for a STAR simulation, it is still prohibitive for Bayesian inference and experimental design, which can require 10^4 model evaluations. To address this, we constructed and verified a surrogate model that ran in seconds.

The construction of the surrogate is summarized in the following four steps:

(i) Generate a Latin Hypercube Sampling (LHS) design to use for surrogate training and run the low-fidelity code (CTF in this study) on this design.

(ii) Generate a LHS design to use for surrogate testing – validate and run the low-fidelity code (CTF this study) on this design.

(iii) Construct the surrogate using the training design.

(iv) Evaluate the surrogate on the test design.

Details regarding the surrogate verification are provided in [5].

3.3.3 Surrogate-Based Bayesian Calibration and CTF Validation

To calibrate one parameter, at least one calibration step must be performed before the experimental design. Furthermore, the use of more experimental data in this initial step yields more informative prior distributions $p(\theta)$ for Bayesian inference. To quantify how the addition of experimental data affected this prior, we performed Bayesian inference using 1, 2, 3 and all 11 calibration experiments. The kernel density estimates (KDE) in Figure 3.7 demonstrate the decrease in uncertainty for β that occurs as data is added. To fully demonstrate the experimental design framework, we employed 1 experiment to initially calibrate β, which yielded a mean value of 0.003197. Subsequent validation demonstrates reduction in the L_2 error from 1.44% to 1.36% thus demonstrating a slight improvement in performance.

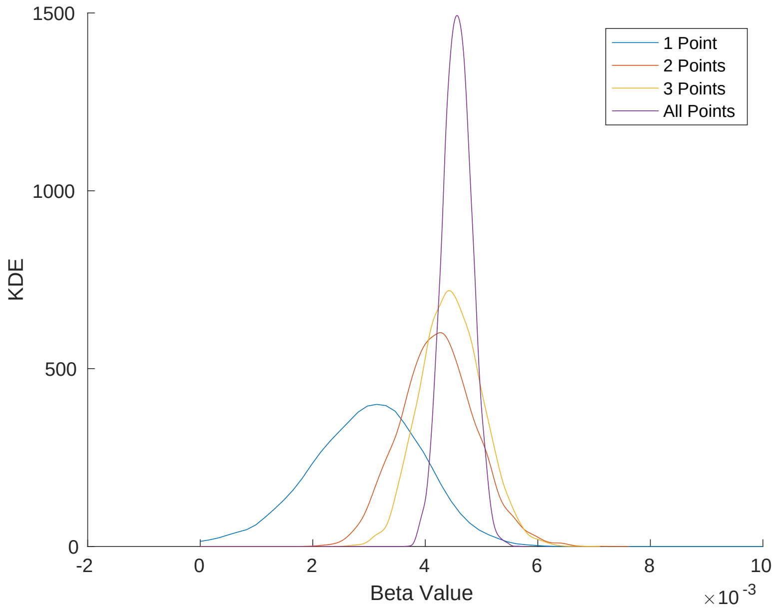

Figure 3.7. Kernel density estimates (KDE) of the distributions for β obtained using 1, 2, 3 and all 11 calibration experiments.

3.3.4 Surrogate-Based Experimental Design and Bayesian Calibration

To initiate the experimental design step summarized in Algorithm˙1, we provided Dakota with a list of candidate designs, the LHS design used in Bayesian calibration, and a calibration data file. The process was performed once with STAR-generated outlet temperatures and once with experimental data. Since STAR runs are expensive, the passing of information between Dakota and STAR was performed offline as a manual process. The functionality to perform this analysis inline, allowing Dakota to drive the high-fidelity simulation runs, is currently in Dakota 6.6 and could be implemented for problems with less intensive high-fidelity codes.

The mutual information (MI) for 20 iterations of the experimental design process with STAR-generated data is plotted in Figure 3.8. While not strictly monotonic, the mutual information generally decreases, as expected. Kernel density estimates of the corresponding distributions for β are plotted in Figure 3.9. It is observed that the initial prior distribution is the most uncertain and the uncertainty decreases as more STAR-generated data is employed. The mean and median β values at iteration 20 are 0.002881.

We repeated this analysis with experimental WEC data and obtained the mutual information and β distributions plotted in Figures 3.10 and 3.11. We note that the distributions converge more quickly to a mean value of 0.004025, which is closer to the WEC proposed nominal value of 0.006, but differs from the mean value 0.002881 computed using STAR-generated data.

The difference between the calibration results using STAR and experimental data highlights the necessity of employing validated high-fidelity codes that represent exactly the same physics as experiment. Analysis in [5] isolates a few mechanisms that can produce discrepancies between the high-fidelity code and experiments, which subsequently yields differences in calibrated parameter values and distributions.

It was first noted that small changes in outlet temperatures can produce changes in β. The nature of the available experimental data makes it difficult to separate the effects due to the physics in the experiment and the effects of geometry and thermocouple mis-calibration.

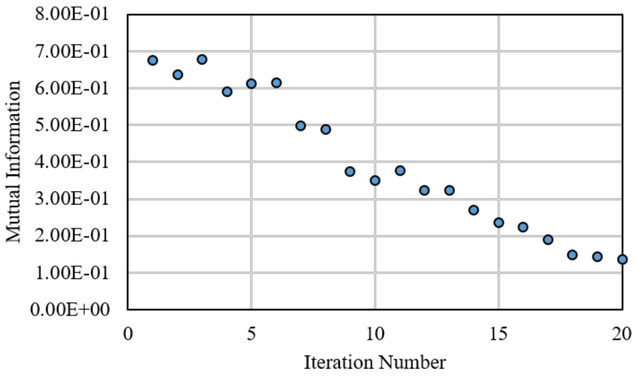

Figure 3.8. Mutual information at each iteration during the STAR experimental design process.

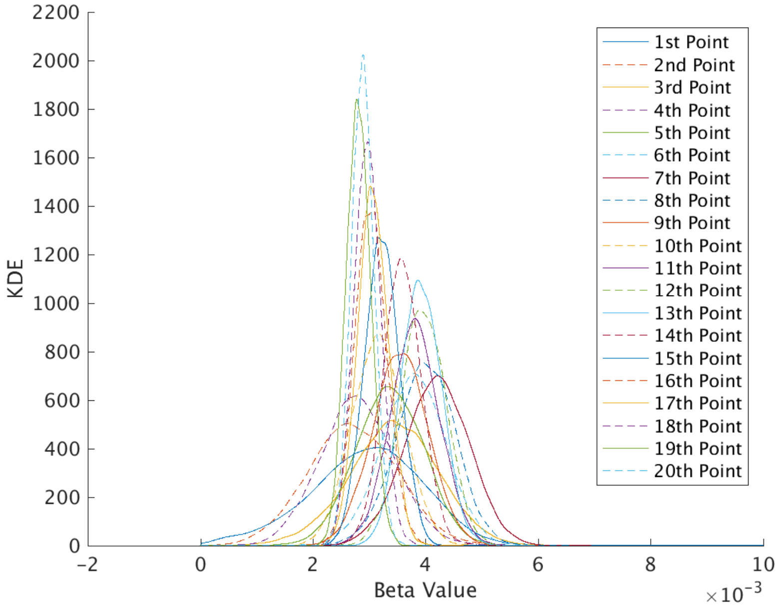

Figure 3.9. Kernel density estimates (KDE) of the distributions for β obtained using 20 iterations of the experimental design framework with STAR data.

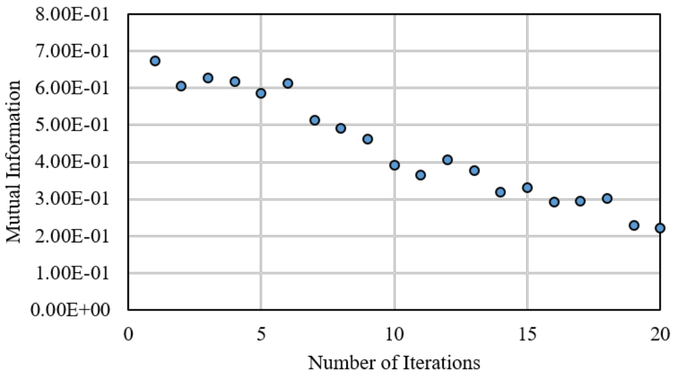

Figure 3.10. Mutual information at each iteration during the experimental design process using experimental data.

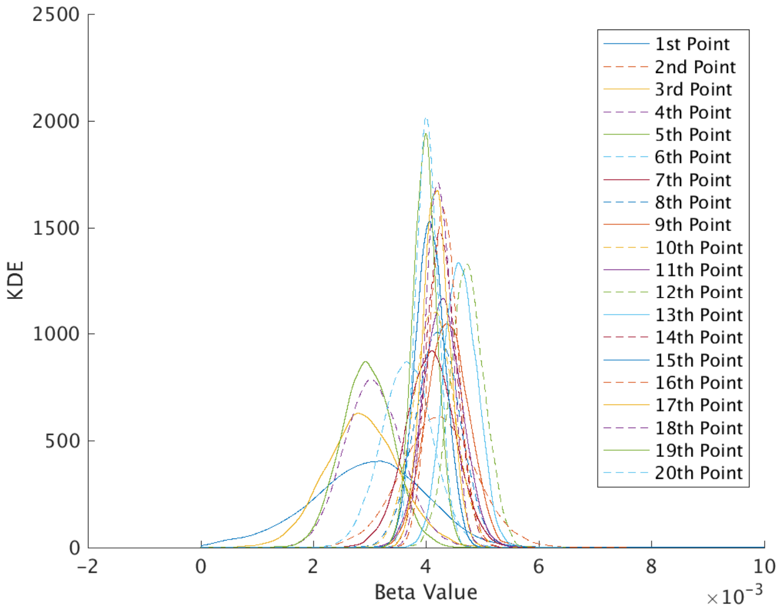

Figure 3.11. Kernel density estimates (KDE) of the distributions for β obtained using 20 iterations of the experimental design framework with experimental data.

Symmetry is a factor leading to the discrepancy observed between STAR and the experiment data points in the Experimental Design step. The STAR and CTF outlet temperatures are symmetric while the experimental outlet temperatures are not symmetric. It is not apparent that the experimental results should be asymmetric. This difference in symmetry should not be confused with the level of turbulent mixing flattening the solution and causing the subchannel temperatures to shift closer to the average temperature. It is not obvious, however, that physical turbulence would result in a lack of symmetry. It is apparent that no calibration of a global β parameter could produce asymmetric results. Asymmetric outlet temperature could only be produced by asymmetric local values of β.

The symmetric discrepancies are shown in Figure 3.12, where the blue dots represent a CTF simulation with no turbulent mixing ($\beta = 0$) and the red dots are a result of a CTF simulation with turbulent mixing ($\beta = 0.004025$). Clearly the blue and red outlet temperatures display symmetry. When the experimental outlet temperatures are added (green dots), the asymmetry of the experimental data is evident. Statistically, the red dots with turbulent mixing are closer to the green dots of the experiment, but for any subchannel it is not clear that the turbulent mixing captures the unresolved physics. Some of the red dots are closer to the green dots than the blue dots and some are further away.

The question is whether the asymmetry in the experiment represents real physics and therefore some of the geometry or physics is missing in STAR, or is caused by asymmetry in the experimental geometry during manufacturing. Since the asymmetry in the experimental data is not easily incorporated in the STAR geometry and mesh, a method for incorporating it in STAR needs to be determined.

Non-physical asymmetry could be caused by poor calibration of the thermocouples in the experiment. Poorly tuned thermocouples can convert a symmetric signal to an asymmetric result. This issue could be resolved by calibrating the thermocouples individually or in groups instead of as a lumped set. Non-physical symmetry could also be caused by damage to the thermocouples imparted during critical heat flux (CHF) experiments performed between turbulent mixing experiments. Calibration of the thermocouples at the beginning of each test could address this issue.

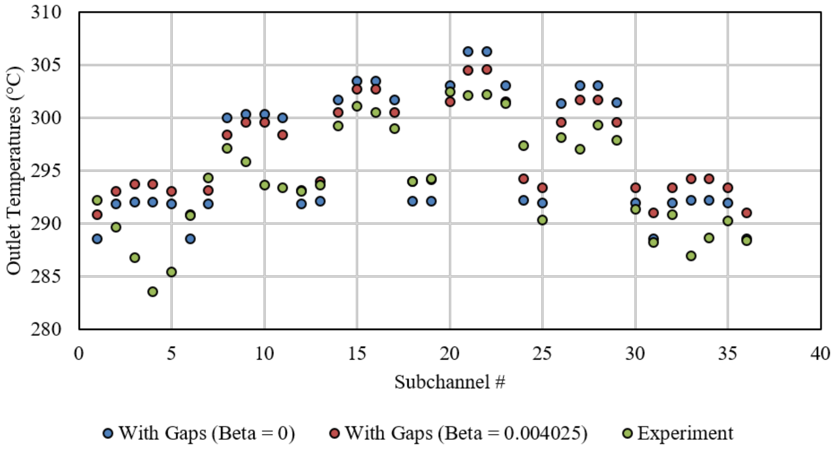

Figure 3.12. Graphical evidence of $\beta' s$ inability to quantify the experimental asymmetry.

3.3.5 Final CTF Validation

A third validation step was performed to determine the improvement in CTF outlet temperatures, when compared to experimental data, as a result of the Experimental Design and Bayesian calibration when all 21 data sets were used to calculate the optimal value of β. As detailed in [5], the resulting L_2 error of 1.36% demonstrates essentially no improvement during the experimental design process. This is due, in part, to the fact that the initial validation using $\beta = 0$ yielded an L_2 error of 1.44% thus indicating minimal room for improvement. We postulate that the biggest reason for not observing more improvement is due to experimental setup. In the experiment the can surrounding the 5 × 5 array was off center. However, CTF assumes that the can is placed symmetrically around the array.

3.4 Conclusions

The work performed in these milestones outlined the steps of the Hi2Lo process. Due to questions regarding the experimental data and STAR, the final results of the analysis, when compared to experimental data, were not as anticipated; however, the goal of demonstrating all steps in the process and reducing the uncertainty in the selected value of β was achieved. While the experimental L_2 norm was not significantly improved by adding 20 additional data points through the Experimental Design process, the uncertainty in β optimal was reduced leading to higher confidence in a value of β optimal. The STAR L_2 norm was improved by adding 20 data points through the Experimental Design process. Differences in outlet temperature symmetry between the codes and the experimental data led to discrepancies in the value of β optimal obtained through an experiment-informed and a STAR-informed Experimental Design process, as well as reducing the improvement made when calculating L_2 norms with respect to the experimental data.

The work performed has demonstrated that it is possible to calibrate β to better align CTF outlet temperatures with the experimental outlet temperatures. Although it is clear that this work improved the fit of CTF outlet temperatures to the experimental data statistically, it is not obvious that adjusting the turbulent mixing parameter in CTF is capturing some unresolved physics.

The ability to calibrate β in CTF to STAR results was also effectively established. Both the STAR outlet temperatures and the CTF outlet temperatures – with and without mixing – are symmetric and the L_2 norm with respect to the STAR data significantly decreases through the Experimental Design process.

In terms of future work, applying the Hi2Lo framework to a problem exhibiting greater sensitivity to at least one of the calibration parameters would be more useful for demonstrating the potential of the process. This implementation of the Hi2Lo process also exposed the reality that high- (and low)-fidelity calculations are often conducted under ideal conditions not often present in physical experiments, potentially leading to statistically significant differences in calibration results between simulations and experiments.

Future work should also be performed to address the symmetry in the code results and the asymmetry in the experimental results. A solution verification also needs to be performed to determine if the error due to the coarseness of the mesh is the culprit in removing the asymmetry from the STAR results. Finally, an investigation into finding a way to change the geometry or physics in the STAR simulation to enable better agreement with the experimental outlet temperatures needs to occur.

Finally, future work will also focus on the use of NESTOR data for the Hi2Lo program. First, we will use NESTOR data to better determine uncertainties in high-fidelity statistical models for STAR. Secondly, we will employ NESTOR data to calibrate and validate heat transfer closure relations in CTF to account for axial temperature distributions. The work will continue as the NESTOR data is released and provided to the CASL partners for the Hi2Lo initiative.

Chapter 4

STAR-Informed Extensions of CTF

Chapter 3 illustrates the complete implementation of the experimental design-based Hi2Lo framework, detailed in Chapter 2, to employ experimental or STAR-generated synthetic data to calibrate the turbulent mixing coefficient β in CTF. Proposed future application of this framework to calibrate fuel components of CTFFuel are summarized in Chapter 5.

Whereas the experimental design-based Bayesian calibration framework constitutes a major component of the Hi2Lo program, it is not the only Hi2Lo initiative in CASL, and a second significant thrust has focused on the use of STAR to inform and improve the turbulence modeling and grid heat transfer modeling capabilities of CTF. We summarize in this chapter a collaborative milestone with Westinghouse, focused on implementing directed crossflow in CTF, and work detailed in the L2:PHI.P15.04 milestone report [18] on the development of a grid heat transfer model for a rod-bundle geometry in CTF.

4.1 STAR-Informed CTF with Westinghouse

The collaborative milestone L3:AMA.P14.04 focused on the use of STAR to improve turbulent modeling capabilities in CTF. This milestone focused primarily on three objectives: (i) determine the variability in STAR temperature predictions introduced through the use of different turbulence models; (ii) calibrate the turbulent mixing coefficient β for experimental mixing vane grid data and quantify the sensitivity of predictions with respect to β, and (iii) add a source term to the liquid lateral momentum equation in CTF to account for directed cross-flow at the subchannel gaps caused by spacer grid mixing vanes. Whereas this milestone did not employ the experimental design-based framework for Bayesian calibration of low-fidelity model parameters, Objectives (i) and (ii) provide a prelude for the analysis in L3:VVI.H2L.P15.01 and L3:VVI.H2L.P15.02 in which we demonstrated the Hi2Lo framework for a non-mixing vane regime; see Chapter 3.

The experimental setup was the same as that detailed in Section 3.1 with the exception that experiments included mixing vane grid spacers such as that shown in Figure 4.1. Details are provided in [6].

As a step toward the quantification of the observation errors $\tilde{\varepsilon}(\xi_n)$ when constructing a high-fidelity statistical model (2.4) for STAR, we quantified how the use of six standard turbulence models affect STAR temperature predictions. The six considered turbulence models are: realizable $k-\varepsilon$ two-layer, realizable $k-\varepsilon$ (high $y+$), linear standard $k-\varepsilon$, quadratic $k-\varepsilon$, cubic standard $k-\varepsilon$, and standard (Wilcox) $k-\varepsilon$. For simulated and experimental temperatures $T_{sim,n}$ and $T_{exp,n}$, for the 36 subchannels, the L_2 norms

$$L_2 = \frac{\sqrt{\sum_{n=1}^{36}(T_{sim,n} - T_{exp,n})^2}}{\sqrt{\sum_{n=1}^{36} T_{exp,n}^2}} \times 100,$$

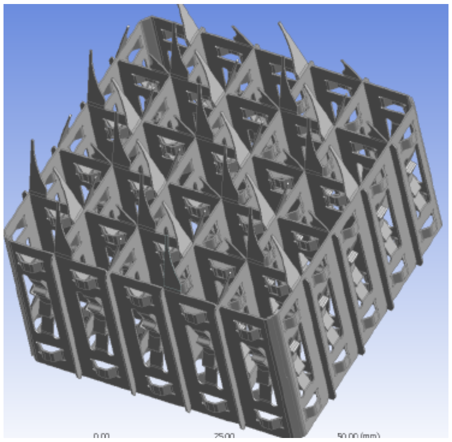

Figure 4.1. CAD representation of the mixing vane grid employed in the 5 × 5 tests.

for the turbulence models are plotted in Figure 4.2 for 11 tests. It is noted that the standard $k - \varepsilon$ model yielded the lowest L_2 norm. However, it should also be noted that these results are mesh-dependent and may change with new meshes. This analysis can be compared with that in Figure 3.5 of Section 3.2.2.

Secondly, we employed deterministic calibration methods in Dakota to compute the optimal β value of 0.037 using the mixing vane grid data. This value can be compared to the mean value 0.004025 computed in Section 3.3.4 using non-mixing vane data. The larger value reflects the fact that β in this case accounts for more mass, momentum and energy transfer between channels due to the mixing vanes. Finally, the sensitivity of normalized temperature predictions to values of β ranging from $\beta = 0.03$ to 0.06 are plotted in Figure 4.3. In Figure 4.4, we illustrate initial comparison of normalized temperatures for CTF with $\beta = 0.037$, STAR and experimental data.

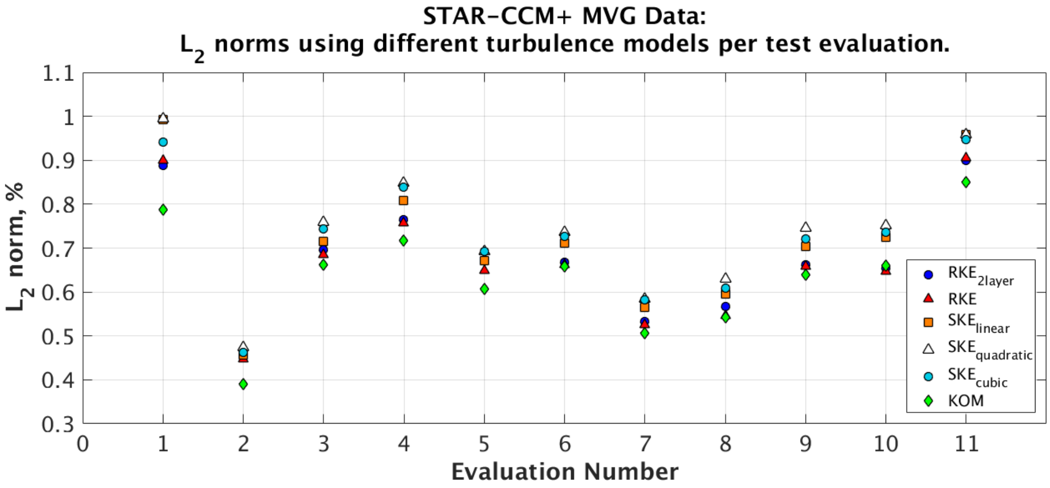

Figure 4.2. Comparison of L_2 norms for 6 turbulence models for a single test case.

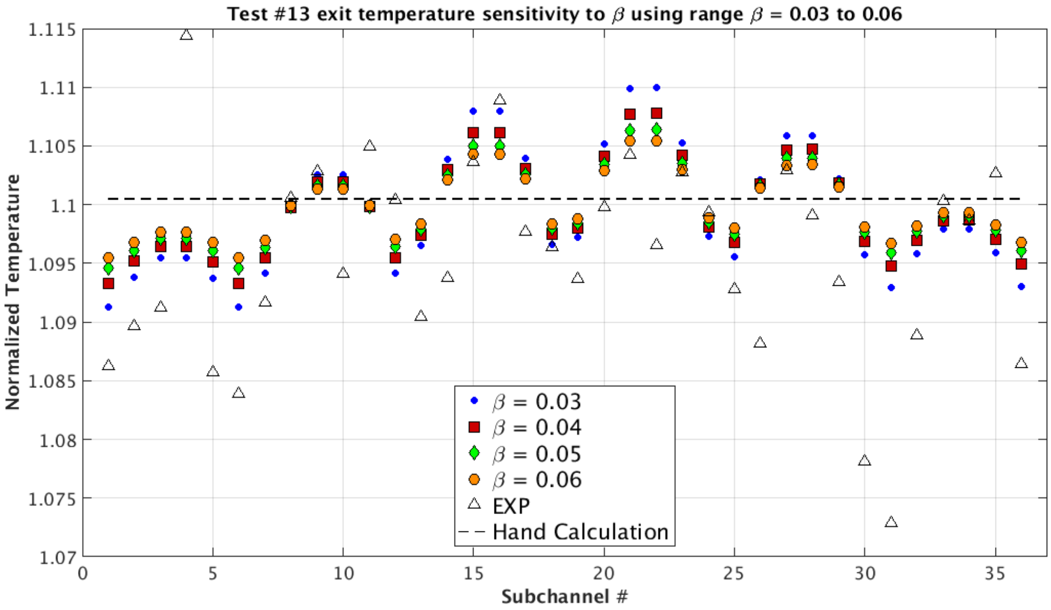

Figure 4.3. Sensitivity of normalized temperatures on β.

As detailed in [6], one objective was improve the functionality of CTF by adding a source term to the liquid lateral momentum equation to account for directed crossflow at the subchannel gaps caused by spacer grid mixing. STAR was used to create multipliers to generate this source term. In Figure 4.5, we illustrate initial normalized temperature comparisons between CTF, with and without directed crossflow, STAR, and experimental data. The addition of directed crossflow introduced a slight amount of asymmetry to the CTF predictions that was not present before; however, the CTF predictions are not necessarily improved compared to the non-crossflow results. In many of the internal subchannels, the addition of the directed cross flow resulted in a worse prediction of experimental temperatures for certain regimes, but the prediction was closer to the experiment/STAR for some of the periphery subchannels.

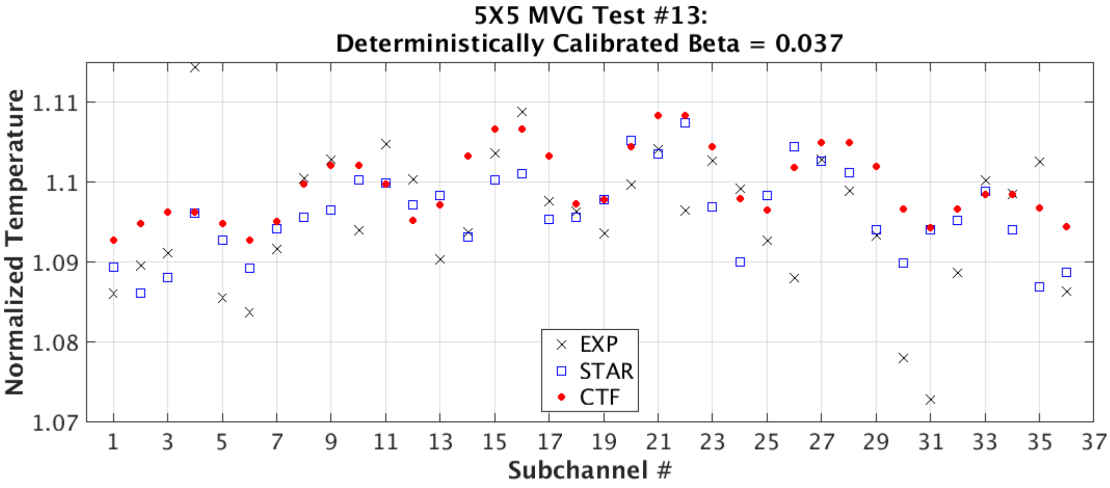

Figure 4.4. Comparison of normalized temperatures for CTF with $\beta = 0.0037$, STAR and experimental data.

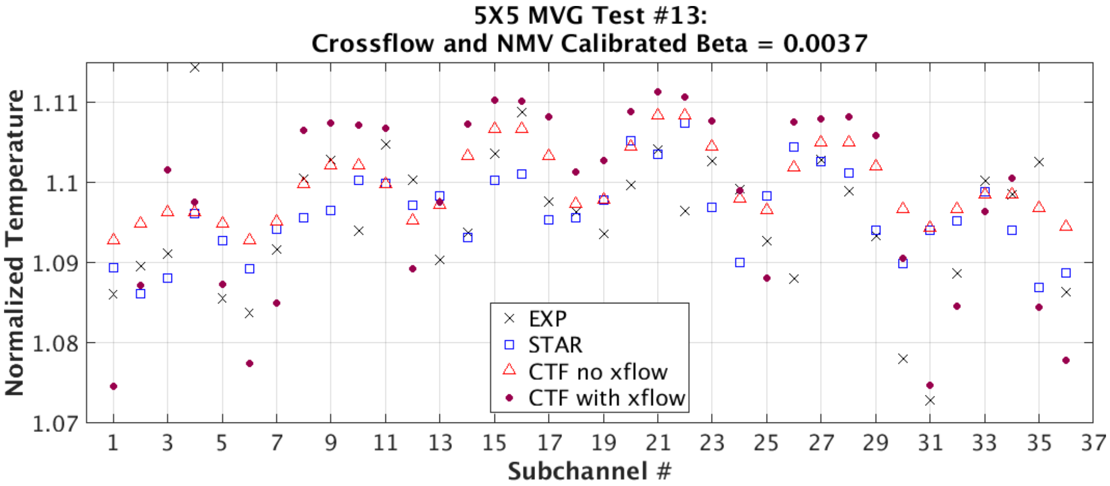

Figure 4.5. Comparison of normalized temperatures for CTF with and without directed crossflow, STAR and experimental data.

This investigation provided an initial step demonstrating the use of the high-fidelity code STAR to improve the grid modeling capabilities of the subchannel code CTF. Future work will focus on creating mixing multipliers, based on STAR, to be added to the turbulent mixing coefficient β in CTF to account for spacer grid-enhanced turbulent mixing within subchannels.

4.2 STAR-Informed Heat Transfer Enhancement in CTF

We summarize here work reported in the L2:PHI.P15.04 milestone report [18], which included the extension of STAR enhanced grid heat transfer modeling capabilities from single-rod level to rod-bundle geometries. Whereas this does not involve the experimental design component of the Hi2Lo framework, it complements the Westinghouse research, discussed in Section 4.1, in the sense that it demonstrates a STAR-informed enhancement of CTF to improve grid modeling capabilities.

Without modification, CTF cannot quantify complex spatially-dependent heat transfer behavior, caused by mixing vane grids, due to its low spatial resolution, lack of advanced turbulence models, and crude representation of the model geometry. The investigation in [19] detailed an approach for developing HTC multiplier maps to reconstruct this grid-generated heat transfer behavior for a single rod. This procedure is extended in [18] to a more realistic rod-bundle geometry, which requires the development of a multiplier map for each pin in the 5 × 5 bundle.

The steps required for this extension can be summarized as follows. CTF was first run without a grid heat transfer model to compute a set of bare-bundle HTC, which could be used to normalize the local HTCs computed using STAR. Secondly, a STAR HTC was computed using the mass-flow-rate-averaged bulk temperature for the adjacent subchannel. For the single-rod case, calculation of the HTC was simplified by the fact that there is only one channel surrounding the rod. The extension to the rod-bundle required the development of Python tools to average the STAR data onto the CTF mesh. After STAR data was used to construct 25 individual rod HTC maps, a shape function was constructed to create the HTC map for the entire length of the pin. The accuracy and performance of the procedure are detailed in [18].

The conclusions in [18] include the following. It is noted that the HTC multiplier maps can only quantify geometry effects of the grid and are not designed to compensate for modeling errors – e.g., represented by $\delta(\xi_n)$ in the statistical model (2.3) – such as deficiencies due to the mixing model. Secondly, it is necessary to first calibrate the turbulent mixing coefficient β since bulk temperature will have a direct linear impact on the predicted rod surface temperature.

Future investigations will focus on extending this feature to production level capabilities. They will also focus on extending the models to accommodate boiling regimes.

Chapter 5

Plans to Calibrate CTFFuel's Deformation Models

The milestone L3:PHI.P15.01 focused on the development of a stand-alone fuel code to simulate steady-state and transient thermo-mechanical responses of light-water reactor fuel rods. It also focused on verifying the temperature predictions using both analytic solutions and a well-established and validated fuel performance code.

The milestone focused on five major topics: (1) development of the code CTFFuel, (2) discussion of the newly implemented fuel deformation models for the dynamic gap conductance model in CTFFuel, (3) integration of the dynamic gap conductance model into VERA-CS, (4) verification of the solid conduction solution and comparison of CTFFuel with respect to the parent code CTF, and (5) benchmarking the thermal conductivity degradation using the burnup-dependent fuel thermal conductivity models and benchmarking the fuel centerline temperature using the dynamic gap conductance model with Halden measurements and FRAPCON-4.0 simulation results. CTFFuel temperature predictions were compared to predictions from FRAPCON-4.0 for UO_2, UO_2+Gd_2O_3 and MOX fuels through the reactor's life. The main motivation was to understand discrepancies between CTFFuel and FRAPCON-4.0's temperature predictions.

In this chapter, we summarize the model development detailed in the milestone report [22], which was developed outside the Hi2Lo initiative, and discuss the future role of the Hi2Lo framework for calibrating parameters in the newly developed fuel models in CTFFuel. Hi2Lo calibration of CTFFuel using BISON generated data will allow VERA to run much faster without having to couple with BISON while maintaining the higher-fidelity of fuel temperatures as predicted by BISON. The verification and validation of the models are detailed in [22].

As motivated in Section 2.1.2, the dynamic gap conductance is given by

$$h_{gap} = h_{gas} + h_{rad} + h_{contact}. \tag{5.1}$$

Here the gas conductivity in the gap h_{gas}, conductance to radiation h_{rad}, and solid-solid contact conductance $h_{contact}$, which incorporates potential physical contact between the fuel pellet and cladding, are given by

$$\begin{aligned} h_{gas} &= \frac{k_{gas}}{D_{mp} + (g_1 + g_2)} = \frac{k_{gas}}{\Delta t_{gap}} \\ h_{rad} &= \sigma_{SB} \frac{(T_f^4 - T_c^4)/(T_f - T_c)}{\frac{1}{\varepsilon_f} + \left(\frac{1}{\varepsilon_c} - 1\right)\frac{A_f}{A_c}} \\ h_{contact} &= C k_m F(L_i, R_i) \left(\frac{P_{int}}{H}\right)^n . \end{aligned} \tag{5.2}$$

Here σ_{SB} denotes the Stefan-Boltzmann constant, T_f, T_c are the fuel surface and clad inside temperatures, A_f, A_c are corresponding areas, ε is the surface emissivity, C is an empirical correlation, and P_{int} is the interfacial pressure. Furthermore, H denotes the Meyer hardness, k is the thermal conductivity, D_{mp} denotes the mean width between the fuel and cladding, $(g_1 + g_2)$ is the temperature jump distance, and Δt_{gap} denotes the gap thickness. In the last relation, $F(L_i, R_i)$ is a function of the peak-to-peak asperity separation L_i and the surface roughness R_i and k_m denotes the mean thermal conductivity.

5.1 Fuel Models

To augment the existing fuel thermal expansion model and to better quantify thermal-mechanical behavior of the fuel rod under LWR conditions, the following new deformation models were implemented in [22]: fuel swelling, fuel irradiation-induced densification, and fuel relocation models. These models all contribute to the change in gap size; a more general relation for the fuel deformation, which contributes to changes in the gap, can be defined as

$$\Delta t_{gap} = t_{init} - \Delta t_{fuel\_thermal\_exp} - \Delta t_{fuel\_swell} - \Delta t_{fuel\_rel} + \Delta t_{fuel\_dens} \tag{5.3}$$

for the gap thickness, which incorporates the strains $\Delta t_{init}, \Delta t_{fuel\_thermal\_exp}, \Delta t_{fuel\_swell}, \Delta t_{fuel\_rel}$ and Δt_{fuel_dens} due to the initial configuration, fuel expansion, fuel swelling, fuel relocation, and fuel irradiation-induced densification.

5.1.1 Fuel Swelling

Fuel swelling is calculated based on the increased volume that fission products must occupy, and is defined as a positive volume change resulting from different solubilities, chemical states, lattice parameters, numbers of atoms, and chemical valences of the atoms resulting from the nuclear fission process [8]. As detailed in [22], two models were implemented in CTF: a MATPRO-11 model and FRAPCON's model for the fuel swelling.

MATPRO Model: The MATPRO-11 model for the swelling S_s due to solid fission products is given in [8] as

$$S_s = 2.5 \times 10^{-29} \Delta Bu \tag{5.4}$$

and swelling S_g due to gaseous fission products for temperatures T below 2800 K is

$$S_g = 8.8 \times 10^{-56} (2800 - T)^{11.73} \exp\left[-0.0162(2800 - T)\right] \cdot \exp\left[-8.0 \times 10^{-27} Bu\right] \Delta Bu. \tag{5.5}$$

Here S_s [$\mathrm{m}^3/\mathrm{m}^3$] is the fractional volume change due to solid swelling, S_g [$\mathrm{m}^3/(\mathrm{fissions}/\mathrm{m}^3)$] is the fractional volume change to gaseous swelling/burnup, Bu [$\mathrm{fissions}/\mathrm{m}^3$] is the total burnup of fuel, ΔBu [$\mathrm{fissions}/\mathrm{m}^3$] is the burnup during a time-step, and T denotes the temperature in degrees K. For fuel temperatures greater than 2800 K, S_g in (5.5) is set to zero.

FRAP Model: FRAPCON has its own swelling model based on the assumption of linear with local (node-average) burnup. It starts after a burnup of 6 GWd/MTU, and accumulates per time-step at a rate equal to 0.062 volume percent per GWd/MTU up to 80 GWd/MTU and 0.086 volume percent per GWd/MTU beyond 80 GWd/MTU [13]. Additionally, gaseous swelling influence on the permanent cladding hoop strain in high burnup rods is given in [13] by

$$\Delta t_{fuel\_swell} = \frac{\Delta \ell}{\ell} = \begin{cases} 4.55 \times 10^{-5} T - 4.37 \times 10^{-2} & , \quad 960^\circ < T < 1370\ ^\circ\mathrm{C} \\ -4.05 \times 10^{-5} T + 7.40 \times 10^{-2} & , \quad 1370^\circ < T < 1832\ ^\circ\mathrm{C}. \end{cases} \tag{5.6}$$

In CTFFuel, it is assumed that swelling is an isotropic deformation, which therefore yields one-third of the volume increase in each direction. There exists differences in the fractional swelling predicted by the two models and the selection of the model is presently left to the user. We note that a better comparison could be performed using existing experimental data.

The parameters in the fuel swelling relation (5.6) were calibrated using Halden integrated reactor data. The re-calibration of these parameters using experimental data in the literature and BISON constitutes a future Hi2Lo calibration task discussed in Section 5.2. To accomplish this, we could consider a fuel swelling relation of the form

$$\Delta t_{fuel\_swell} = \begin{cases} \theta_1 T + \theta_2 & , \quad 960\ ^\circ\mathrm{C} < T < \theta_4 \\ \theta_3(T - \theta_4) + \theta_2 + \theta_1\theta_4 & , \quad \theta_4 < T < 1832\ ^\circ\mathrm{C}, \end{cases} \tag{5.7}$$

where $\theta = [\theta_1, \ldots, \theta_4]$ are parameters to be inferred using experimental or BISON-generated synthetic data.

5.1.2 Fuel Irradiation-Induced Densification

The dimensional changes in fuel due to irradiation-induced densification of UO_2 fuel is calculated during the first few thousand hours of water reactor operation. The densification is computed as a function of fuel burnup, temperature, and initial density. As detailed in [22], three fuel densification models are implemented in CTF: a MATPRO-11 model, a FRAP model and an ESCORE model.

MATPRO/FRAP Model: As detailed in [8,13], MATPRO-11/FRAP models calculate the total densification

$$\Delta t_{fuel\_dens} = \frac{\Delta L}{L_0} = \left(\frac{\Delta L}{L_0}\right)_m + \exp\left(-3.0(Bu + B)\right) + 2.0\exp\left(-35.0(Bu + B)\right) \tag{5.8}$$

as a function of burnup. Here $(\Delta L/L_0)_m$ denotes the maximum possible change in fuel due to irradiation, Bu [$^{\mathrm{MWd}}/_{\mathrm{kgU}}$] is fuel burnup and B is a constant determined by a numerical algorithm with the boundary condition $\Delta L/L_o = 0$ when $Bu = 0$.

The maximum possible dimension change of fuel due to irradiation $(\Delta L/L_0)_m$ is specified as follows. If a nonzero resintering density change $\Delta\rho_D$, with units of [$^{\mathrm{kg}}/_{\mathrm{m}^3}$], is employed as an input, the dimension change is given by

$$\left(\frac{\Delta L}{L_o}\right)_m = \begin{cases} -0.00150 \cdot \Delta\rho_D & , \quad T < 1000\ \mathrm{K} \\ -0.00285 \cdot \Delta\rho_D & , \quad T \geq 1000\ \mathrm{K}, \end{cases} \tag{5.9}$$

where T denotes temperature in degrees K. For the case when it is not employed as an input, then

$$\left(\frac{\Delta L}{L_o}\right)_m = \begin{cases} -\frac{22.2(100-TD)}{(T_{SINT}-1453)} & , \quad T < 1000\ \mathrm{K} \\ -\frac{66.6(100-TD)}{(T_{SINT}-1453)} & , \quad T \geq 1000\ \mathrm{K}, \end{cases} \tag{5.10}$$

where TD [%] is the theoretical density and T_{SINT} is the sintering temperature in degrees K.

In contrast to MATPRO-11, FRAPCON-4.0 calculates the maximum possible fuel dimension change due to irradiation, with non-zero resintering density change as an input, using the relation

$$\left(\frac{\Delta L}{L_o}\right)_m = \frac{100 \cdot RSNTR}{(3.0 \cdot FDENS)}; \tag{5.11}$$

see [13] for details.

ESCORE Model: In this model, it is shown in [17] that the total accrued specific volume change $\left(\frac{\Delta V}{V_0}\right)_D$, due to densification at a constant temperature operation, is given by

$$\left(\frac{\Delta V}{V_0}\right)_D = \Delta\rho_D \left[\exp\left\{Bu \cdot \frac{\ln(0.10)}{CBu_D}\right\}\right] \tag{5.12}$$

for temperature-independent densification, where $C = 1.0$. For temperature-dependent densification, one employs the relation

$$C = \begin{cases} 1.0 & , \quad T_f \geq 750 \text{ °C} \\ 7.2 - 4.3(T_f - 25)/500 & , \quad T_f < 750 \text{ °C}, \end{cases} \tag{5.13}$$

where $\Delta\rho_D$ [%] denotes the total amount of densification that can occur as a fraction of theoretical density and Bu_D is the burnup at which densification is complete.

5.1.3 Fuel Relocation

FRAP Model: The fuel relocation model, which computes the change in pellet outer diameter, is a function of burnup and power and is given in [13] by

$$\begin{aligned} \Delta t_{fuel\_rel} &= \tfrac{\Delta D}{D_0} \\ &= \begin{cases} 0.055 & , \quad Bu < 0.0937 \,\text{GWd/MTU} \\ 0.055 + \min\left(C_R, C_R \cdot [0.5793 + 0.2447\ln(Bu)]\right) & , \quad Bu \geq 0.0937 \,\text{GWd/MTU}, \end{cases} \end{aligned} \tag{5.14}$$

where

$$C_R = \begin{cases} 0.345 & , \quad q' < 20 \\ 0.345 + (q' - 20)/200 & , \quad 20 \leq q' \leq 40 \\ 0.445 & , \quad q' > 40. \end{cases} \tag{5.15}$$

Here $\Delta D/D_0$ notes the fraction of the gap closure due to relocation to as-fabricated gap closure, q' [kW/ft] denotes the local power, and Bu [GWd/MTU] is the local burnup.

As with the fuel swelling model (5.6), the relocation model (5.14) and (5.15) contains a number of parameters that were calibrated using Halden data. For future CASL applications, we will consider general relations

$$\Delta t_{fuel\_rel} = \begin{cases} \theta_1 & , \quad Bu < \exp(-\theta_2/\theta_3) \\ \theta_1 + \min\left(C_R, C_R \cdot [\theta_2 + \theta_3\ln(Bu)]\right) & , \quad Bu \geq \exp(-\theta_2/\theta_3), \end{cases} \tag{5.16}$$

where

$$C_R = \begin{cases} \theta_4 & , \quad q' < \theta_6 \\ \theta_4 + (q' - \theta_6)/\theta_5 & , \quad \theta_6 \leq q' \leq \theta_7 \\ \theta_4 + (\theta_7 - \theta_6)/\theta_5 & , \quad q' > \theta_7. \end{cases} \tag{5.17}$$

Here $\theta = [\theta_1, \ldots, \theta_7]$ are parameters that will be calibrated using the Hi2Lo framework with experimental data or synthetic data generated using BISON.

ESCORE model The fuel relocation model to calculate the change in pellet outer diameter is given in [17] by

$$\left(\frac{\%\Delta D}{D_0}\right)_{REL} = 0.80Q\left(\frac{\%G_t}{D_0}\right)\left(0.005Bu^{0.3} - 0.20D_0 + 0.3\right), \tag{5.18}$$

where

$$Q = \begin{cases} 0.0 & , \quad q' \leq 6 \\ (q'-6)^{1/3} & , \quad 6 < q' \leq 14 \\ (q'-10)^{1/2} & , \quad q' > 14. \end{cases} \tag{5.19}$$

In this case, $(\%\Delta D/D_0)_{REL}$ is the percent change in diameter due to relocation, D_0 [in] denotes the as-fabricated cold diameter of the fuel pellet, Bu $[\mathrm{MWd}/\mathrm{MTU}]$ is the pellet average fuel burnup, and G_t [in] denotes the as-fabricated cold gap diameter, which is the initial gap thickness.

5.2 Future Hi2Lo Calibration of CTFFuel Parameters

The forms of deformation models are selected similar to FRAP models to facilitate calibration. These models must all be validated and, most likely be re-calibrated, before CTFFuel can be integrated into VERA.

In FY18, we will employ the Hi2Lo experimental design and Bayesian calibration framework to calibrate relevant parameters θ – e.g., see (5.6), (5.16) and (5.17) – using both experimental data available in the literature and BISON-generated synthetic data. Whereas the MATPRO and EXCORE relations are also employed in BISON, the predictions provided by CTFFuel and BISON will likely differ, in part due to the respective finite-difference and finite-element implementations. We will employ the experimental data to quantify discrepancies in BISON predictions due to missing physics when quantifying gaps between cladding and fuel. We will subsequently employ the experimental design framework to determine where in the design space to evaluate BISON to optimally provide information when calibrating parameters in closure relations.

Chapter 6

Conclusions and Future Work

This report documents several CASL initiatives broadly focused on the use of validated high-fidelity simulation codes to inform, improve and calibrate low-fidelity codes to facilitate multiphysics coupling, design, performance analysis, and risk assessment. During the last year, there were two primary components to the program: demonstration of the experimental design-based Bayesian calibration framework to calibrate the turbulent mixing coefficient β in CTF using both STAR-generated synthetic data and experimental data, and the use of STAR to inform and improve the turbulence modeling and grid heat transfer modeling capabilities in CTF. A complementary milestone focused on the implementation and verification of fuel models in CTFFuel, for which we demonstrated initial calibration results.

The demonstration of the experimental design-based Bayesian calibration framework illustrated that it is possible to calibrate β to better align CTF outlet temperatures with the experimental outlet temperatures. Although it is clear that this work improved the fit of CTF outlet temperatures to the experimental data statistically, it is not obvious that adjusting the turbulent mixing parameter in CTF is quantifying some unresolved physics. The ability to calibrate β in CTF to STAR results was also effectively established. Both the STAR outlet temperatures and the CTF outlet temperatures, with and without mixing, are symmetric and the L_2 norm with respect to the STAR data significantly decreases through the experimental design process.

In future work, we will perform sensitivity analysis studies with CTF to identify important parameters that induce variations in subchannel temperatures along the axial domain. Future work should also address the fact that the codes produced symmetric results whereas the experimental data exhibited asymmetries. A solution verification also needs to be performed to determine if the error due to the coarseness of the mesh is the culprit in removing the asymmetry from the STAR results. Finally, we need to investigate how to change the geometry or physics in the STAR simulation to enable better agreement with the experimental outlet temperatures.

The investigations focused on employing STAR to inform CTF produced a directed cross-flow model and STAR-enhanced grid heat transfer model for rod-bundle geometries. Future work will focus on creating mixing multipliers, based on STAR, to be added to the turbulent mixing coefficient β in CTF to account for spacer grid-enhanced turbulent mixing within subchannels.

Future work will also focus on the use of NESTOR data for Hi2Lo applications. We will first use NESTOR data to better determine uncertainties in high-fidelity statistical models for STAR. Secondly, we will employ NESTOR data to calibrate and validate heat transfer closure relations in CTF to account for axial temperature distributions. The work will continue as the NESTOR data is released and provided to the CASL partners for the Hi2Lo initiative.

Finally, a significant component of the future Hi2Lo program will focus on the use of the Hi2Lo experimental design framework to calibrate parameters in the developed fuel swelling, fuel irradiation-induced densification, and fuel relocation models in CTFFuel using both experimental and BISON-generated data. We will also employ experimental data to quantify discrepancies in BISON predictions due to missing physics when quantifying gaps between cladding and fuel.

Acknowledgments

This research is supported by and performed in conjunction with the Consortium for Advanced Simulation of Light Water Reactors (http://www.casl.gov), an Energy Innovation Hub (http://www.energy.gov/hubs) for Modeling and Simulation of Nuclear Reactors under U.S. Department of Energy Contract No. DE-AC05-00OR22725.

The following individuals made substantial contributions to material that supported this milestone: Brian Adams (SNL), Marc-Oliver Delchini (ORNL), Will Gurecky (University of Texas), Annalisa Manera (University of Michigan), Kathryn Maupin (SNL), Victor Petrov (University of Michigan), David Pointer (ORNL), Stuart Slattery (ORNL), Laura Swiler (SNL), Daniel Walter (University of Michigan), Xingang Zhao (MIT)

Bibliography

[1] B.M. Adams, R.W. Hooper, A. Lewis, R.C. Smith, L.P. Swiler and B.J. Williams, “User guidelines and best practices for CASL VUQ analysis using Dakota,” CASL Report CASL-X-2014-0038-000.

[2] C. Bryant and G. Terejanu, “An information-theoretic approach to optimally calibrate approximate models”, *American Institute of Aeronautics and Astronautics*, 2012.

[3] K.D. Coleman, R.C. Smith, B. Williams and M. Morris, “An initialization algorithm for gradient-free active subspace construction,” CASL Report CASL-U-2017-1449-000.

[4] L. Gilkey, “STAR-CCM+ (CFD) calculations and validation,” CASL Report CASL-U-2017-1421-000.

[5] N. Gordon, ‘CTF (subchannel) calculations and validation,” CASL Report CASL-U-2017-1420-000.

[6] N. Gordon, L. Gilkey, T. Blyth, R.C. Smith, E. Tatli and Y. Sung, “Initial application of Hi2Lo approach to turbulent mixing model improvement,” CASL Report CASL-U-2017-1292-000.

[7] H. Haario, M. Laine, A. Mira and E. Saksman, “DRAM: Efficient adaptive MCMC,” *Statistics and Computing*, 16(4), pp. 339–354, 2006.

[8] D.L. Hagrman and G.A. Reymann and R.E. Manson, *MATPRO-Version 11 (Revision 1): A Handbook of Materials Properties for Use in the Analysis of Light Water Reactor Fuel Rod Behavior*, USNRC Report NUREG/CR-0497, TREE-1290, Idaho National Engineering Laboratories, February, 1980.

[9] A. Kraskov, H. Stogbauer and P. Grassberger, “Estimating mutual information”, *Physical Review E*, 69(6), 2004.

[10] A. Lewis, R.C. Smith and B. Williams, “Bayesian model calibration on active subspaces,” Proceedings of the American Control Conference (ACC), May 24-26, 2017, Seattle, WA CASL Report CASL-U-2017-1450-000.

[11] A. Lewis, R.C. Smith, B. Williams and V. Figueroa, “An information theoretic approach to use high-fidelity codes to calibrate low-fidelity codes,” *Journal of Computational Physics*, 324, pp. 24–43, 2016.

[12] J. Liepe, S. Filippi, M. Komorowski and M.P.H. Stumpf, “Maximizing the information content of experiments in systems biology”, *PLOS Computational Biology*, 9(1), Jan. 2013.

[13] W.G. Luscher and K.J. Geelhood and I.E. Porter, *Material Property Correlations: Comparisons between FRAPCON-4.0, FRAPTRAN-2.0, and MATPRO*, Technical Report PNNL-19417 Rev. 2, Pacific Northwest National Laboratory, September 2015.

[14] J.A. McMahan, Jr., B.J. Williams, R.C. Smith and N. Malaya, “A linear regression framework for the verification of Bayesian model calibration algorithms,” *Journal of Verification, Validation and Uncertainty Quantification*, 2, 021006-1, 2017; CASL Report CASL-U-2017-1452-000.

[15] I.J. Michaud, B.J. Williams and R.C. Smith, "Mutual information estimation for simulation-based high-to-low calibration," CASL Report CASL-U-2017-1451-000.

[16] F. Morris and W. Whitman, "Heat transfer for oils and water in pipes," *Industrial and Engineering Chemistry*, 20(3), pp. 234–240, 1928.

[17] Y. Rashid and R. Dunham and R. Montgomery, *Fuel Analysis and Licensing Code: FALCON MOD01*, Technical Report EPRI 1011308, Electric Power Research Institute, December 2004.

[18] R. Salko, M-O. Delchini, X. Zhao, D. Pointer and W. Gurecky, "Summary of CTF accuracy and fidelity improvements in FY17," CASL Report CASL-U-2017-1428-000.

[19] R. Salko, W. Gurecky, S. Slattery, K. Clarno, D. Pointer, D. Walter, V. Petrov and A. Manera, "Implementation of a grid heat transfer and turbulent kinetic energy Hi2Lo remapping capability in CTF in support of the CIPS challenge problem," CASL Report CASL-U-2017-1322-000.

[20] R.C. Smith, *Uncertainty Quantification: Theory, Implementation and Applications*, SIAM, Philadelphia, 2014.

[21] G. Terejanu, R.R. Upadhyay and K. Miki, "Bayesian experimental design for the active nitration of graphite by atomic nitrogen", *Experimental Thermal and Fluid Science*, Vol. 36, Jan. 2012, pp. 178-193.

[22] A. Toptan, R.K. Salko, M.N. Avramova, D.J. Kropaczek and K. Clarno, "Development and Assessment of CTFFuel," CASL Report CASL-U-2017-1418-000.